Microsc. Microanal. 18, 915–940, 2012
doi:10.1017/S1431927612001468

Microscopy AND Microanalysis

REVIEW ARTICLE

What Remains to Be Done to Allow Quantitative X-Ray Microanalysis Performed with EDS to Become a True Characterization Technique?

Raynald Gauvin*

Department of Materials Engineering, McGill University, M.H. Wong Building, 3610 University Street, Montréal, Québec H3A 2B2, Canada

Abstract: This article reviews different methods used to perform quantitative X-ray microanalysis in the electron microscope and also demonstrates the urgency of measuring the fundamental parameters of X-ray generation for the development of accurate standardless quantitative methods. Using ratios of characteristic lines acquired on the same X-ray spectrum, it is shown that the Cliff and Lorimer $K_{A\text{-}B}$ factor can be used in a general correction method that is appropriate for all types of specimens and electron microscopes, providing that appropriate corrections are made for X-ray absorption, fluorescence, and indirect generation. Since the fundamental parameters appear in the $K_{A\text{-}B}$ factor, only the ratio of the ionization cross sections needs to be known, not their absolute values. In this regard, the measurement of ratios of the $K_{A\text{-}B}$ factor (or intensities at different beam energies of the same material with no change of beam spreading in the material) permits the validation for the best models to compute the ratio of ionization cross sections. It is shown, using this method, that the nonrelativistic Bethe equation, to compute ionization cross section, is very close to the equation of E. Casnati et al. (*J Phys B* **15**, 155–167, 1982) and also to the equations proposed by D. Bote and F. Salvat (*Phys Rev A* **77**, 042701, 2008) for the computation of the ratio of ionization cross sections. The method is extended to show that it could be used to determine the values of the Coster-Kronig transitions factors, an important fundamental parameter for the generation of L and M lines that is mostly known with poor accuracy. The detector efficiency can be measured with specimens where their intensities were measured with an energy dispersive spectrometer detector, the efficiency of which has been measured in an X-ray synchrotron (M. Alvisi et al., *Microsc Microanal* **12**, 406–415, 2006). The spatial resolution should always be computed when performing quantitative X-ray microanalysis and the equations of R. Gauvin (*Microsc Microanal* **13**(5), 354–357, 2007) for bulk materials and the one presented in this article for thin films should be used. The effects of X-rays generated by fast secondary electrons and by Auger electrons are reviewed, and their effect can be detrimental for the spatial resolution of materials involving low-energy X-ray lines, in certain specific conditions. Finally, quantitative X-ray microanalysis of heterogeneous materials is briefly reviewed.

Key words: X-ray microanalysis, electron microscopy, Monte Carlo simulations, ionization cross sections, Coster-Kronig transition factors, fast secondary electrons, Auger electrons, spatial resolution

Introduction

The origin of quantitative X-ray microanalysis in electron microscopy started with the work of Castaing (1951), who built the first electron microprobe and developed the first correction procedure in his seminal PhD thesis. Castaing developed the electron microprobe using the wavelength dispersive spectroscopy (WDS) technique to detect characteristic X-rays. Since each characteristic X-ray line has a well-defined energy, it has therefore a well-defined wavelength that gives a specific diffraction angle for a given crystal using Bragg's law. In WDS, the detection of a characteristic line is performed by tilting a crystal to the corresponding Bragg angle. Also, Castaing developed the basic principle of quantitative X-ray microanalysis, consisting of normalizing the net intensity, I_i, of a characteristic X-ray line of an element i measured in a material composed of many elements of unknown concentration c_i to $I_{(i)}$, that obtained under the same experimental conditions in a material where the concentration of element i, $c_{(i)}$, is known. The normalization of the net intensity of each element to that obtained with standards of known composition has been proven to be very effective for reducing uncertainties in the fundamental parameters needed to compute absolute X-ray generation.

In his thesis, Castaing introduced the concept of the curves of X-ray generation, the $\varphi(\rho z)$ curves, to derive the absorption correction, A_i, to correct for the difference of X-rays absorbed in the specimen of unknown composition from that of the standard. Duncumb (1957) introduced the atomic number correction, Z_i, to correct for the difference of X-rays generated in the specimen of unknown composition from that of the standard. Finally, the fluorescence correction, F_i, was introduced to correct for the differences

Received May 28, 2011; accepted May 7, 2012
*E-mail: raynald.gauvin@mcgill.ca

of X-rays fluoresced in the specimen of unknown composition from that of the standard, using an expression for the characteristic fluorescence developed by Reed (1965) and an expression for the bremsstrahlung fluorescence developed by Henoc (1968). These corrections factors led to the well-known ZAF method that relates the weight fraction, c_i, of each element i in the unknown to the measured intensities through the following equation (Goldstein et al., 2003):

$$\frac{c_i}{c_{(i)}} = Z_i A_i F_i \frac{I_i}{I_{(i)}}, \tag{1}$$

where equation (1) is solved iteratively for each element until convergence is obtained. An excellent review of the ZAF method is given in the classic textbook of Goldstein et al. (2003). The parameters that must be kept constant during the measurement of I_i and $I_{(i)}$ for all elements i, to ensure that the differences are related to composition changes only, are the electron beam energy, the take-off angle of the X-ray detector, the acquisition time, and the beam current. Since the concentrations of all the elements in the unknown specimen are determined independently, or through known stoichiometric ratios if not measured (as might be the case for certain low Z elements), their summation must be equal to 100% to obtain a successful analysis. In modern electron microprobes, the accuracy in the determination of each element can be as good as 1%, which makes this method the most accurate spectrometry technique to perform absolute quantitative chemical analysis of materials with a spatial resolution at the μm level.

Despite this impressive achievement, quantitative X-ray microanalysis is not used on a day-to-day basis by the vast majority of microscopists who acquire energy dispersive spectrometer (EDS) spectra in electron microscopes. The first reason is that the current models of equation (1) were developed mostly for specimens of homogeneous composition and a flat surface. Most materials analyzed in the scanning electron microscope (SEM) do not have locally homogeneous composition or a flat surface, which is a serious limitation, and it is disappointing that manufacturers still only offer quantitative software packages for homogeneous materials. The second reason is the fact that quantitative X-ray microanalysis was developed for a specific instrument—the electron microprobe that was first built by Castaing (1951) and led to its subsequent commercialization. The electron microprobe was designed as a quantitative X-ray microanalysis tool to perform quantitative analysis, not imaging. The SEM was designed to be an imaging tool, not a quantitative X-ray microanalysis tool. With the introduction of the energy dispersive X-ray spectrometers made with lithium-drifted silicon detectors [Si(Li)] by Fitzgerald et al. (1968), detection of X-rays became a possibility in the SEM and in the transmission electron microscope (TEM). However, since the Si(Li) EDS detectors were installed on instruments designed mostly for imaging, quantitative X-ray microanalysis remained used mostly in the microprobes for bulk specimens. In the TEM, quantitative analysis is a method used mostly in expensive dedicated analytical instruments that came into use in the 1980s.

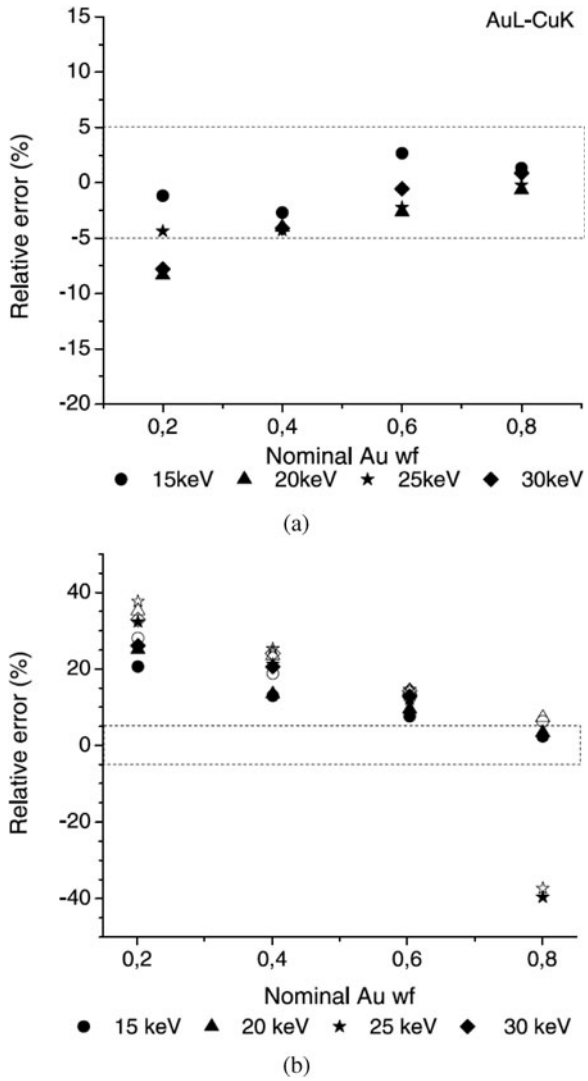

Figure 1. Relative error of estimation of the Au weight fraction with (**a**) the new quantitative X-ray microanalysis method of Horny et al. (2010) and (**b**) a commercial standardless X-ray microanalysis method using the NIST SRM 482 Cu-Au standard. Figures from Horny et al. (2010).

The third reason is that to perform quantitative X-ray microanalysis, standards are needed to acquire reference spectra, and this is time-consuming. Most SEM users do not have a strong background in the experimental and theoretical details of quantitative X-ray microanalysis, and they prefer to push a button to perform it. Despite manufacturers' claims, standardless quantitative X-ray microanalysis is often less accurate than that performed with standards, as shown by Newbury et al. (1995) and Horny et al. (2010). Figure 1 compares quantitative X-ray microanalysis of the NIST SRM–482 Cu–Au standard obtained by a method using standards with a commercial standardless method. The accuracy of the quantitative method using standards is better than 5% while that of the commercial standardless method is around 20%. This is the current state-of-the-art

with standardless quantitative X-ray microanalysis. I claim strongly that without accurate standardless quantitative X-ray analysis developed for the best SEM and TEM for characterizing real materials, quantitative X-ray microanalysis will remain the property of a very select club of experts of high caliber—not a tool to solve real problems, but only to perform elemental identification and qualitative chemical mapping. Even worse, the lack of an accurate standardless method can only generate incorrect data that will ultimately undermine the field of quantitative X-ray microanalysis.

This article is organized as follows. First, the classical quantitative X-ray microanalysis methods are reviewed in the SEM and in the TEM. Second, the new quantitative X-ray microanalysis method proposed by Horny et al. (2010) is presented to demonstrate how it could unify quantitative X-ray microanalysis in the SEM and in the TEM. Third, the problems that need to be solved to develop a standardless quantitative X-ray method are presented. The accuracy of the fundamental parameters is reviewed, and the utility of measuring Cliff and Lorimer (1975) $K_{A\text{-}B}$ factors at different accelerating voltages (or intensities at different beam energies of the same material with no change of beam spreading in the material) to compute the ratio of ionization cross sections is presented, following the work of Gauvin (1990). That method is extended to show that it could be used to determine the value of the Coster-Kronig transition factor, an important fundamental parameter for the generation of L and M lines that is mostly known with poor accuracy. The measurement of the detector efficiency follows, and the road to standardless quantitative X-ray microanalysis is reviewed. Then, the spatial resolution of X-ray microanalysis is presented, in the SEM and as well as in the TEM. The effects of X-rays generated by fast secondary electrons (FSE) and by Auger electrons are reviewed, and their effect can be detrimental for the spatial resolution of materials involving low energy X-ray lines—also inaccurate quantification might occur if their effects are not taken into account. Finally, quantitative X-ray microanalysis of heterogeneous materials is briefly reviewed.

X-Ray Intensity Emitted from a Homogeneous Thick Solid

The net X-ray intensity of a characteristic line of an element i, I_i, emitted from a thick specimen can be computed by this equation:

$$I_i = \left(\frac{\Omega}{4\pi}\right)\frac{i_p\tau}{e}\,Q_i\,\omega_i\,\alpha_i(1+T_{CK,i})\,\varepsilon_i\,\frac{c_i}{A_i} \times N_0\,\gamma_i\left(1+\left\{\sum_{j=1}^{m} f_{c,j}\right\}+f_{Br}+f_{ind}\right), \quad (2)$$

where

$$\gamma_i = \int_0^{\infty} \phi(\rho z)_i \exp(-\chi_i\,\rho z)\,d\,\rho z. \quad (3)$$

$(\Omega/4\pi)$ is the fractional solid angle of the X-ray detector, i_p is the electron beam current, τ is the acquisition time, e is the electron charge, Q_i is the ionization cross section of the atomic shell from which the characteristic line of element i originates and is computed for the incident electron energy E_0, ϖ_i is the fluorescence yield of the ionized atomic shell of element i, and α_i is the weight of the characteristic line of element i. The $(1 + T_{CK,i})$ factor accounts for the effect of Coster-Kronig transitions on X-ray emission for the ionized atomic shell of element i. $T_{CK,i} = 0$ for the K lines. ε_i is the detector efficiency for the characteristic line of element i, C_i is the composition given as the weight fraction of element i in the thick specimen, A_i is the atomic weight of element i, and N_0 is Avogadro's number. $f_{c,j}$ is the contribution of fluorescence on I_i from the m characteristic lines having photon energy greater than the characteristic line i, and this term is significant only for X-rays having their energy slightly greater than the energy of the characteristic line i. f_{Br} is the contribution of fluorescence on I_i from the bremsstrahlung photons having an energy greater than the energy of the characteristic line of the element i. f_{Br} is generally negligible when the absorption correction, described below, is between 0.95 and 1.05. f_{ind} is the fraction of X-rays generated by stray electrons, backscattered electrons, FSEs, and/or Auger electrons contributing to I_i. The contributions of FSEs and Auger electrons are reviewed below.

In equation (3), $\varphi(\rho z)_i$ is the function of X-ray generation for the ionized shell of element i in a thick material as a function of the mass depth ρz, where z is the depth from the surface of the specimen and ρ is the mass density—the interested reader is referred to the book of Goldstein et al. (2003) for a complete description of this function. The $\varphi(\rho z)$ function is multiplied by an exponential function that depends on $\chi_i \rho z$ to account for X-ray absorption, and this product is integrated from 0 to infinity as a function of ρz for a bulk specimen. The terms in front of the integral γ_i in equation (2) (except for the fluorescence and indirect generation corrections) correspond to the thin film contribution per mass thickness on X-ray generation, and the integral γ_i corresponds to the contribution of the bulk specimen on X-ray emission. In the absorption function, χ_i is given by the equation:

$$\chi_i = \operatorname{cosec}\psi \sum_{j=1}^{n} C_j \left.\frac{\mu}{\rho}\right|_j^i, \quad (4)$$

where the summation is taken for the n elements of the specimen, $\mu/\rho|_j^i$ is the mass absorption of the characteristic line of element i into the absorbing element j, and ψ is the take-off angle of the X-ray detector.

X-Ray Intensity Emitted from a Homogeneous Thin Film

For a thin foil, $f_{c,j}$, f_{Br}, and f_{ind} become negligible (at least for a cube of very small thickness) and $\varphi(\rho z)_i = 1$, by definition. Also, since ρz is small, i.e., $\chi_i \rho z \ll 1, \exp(-\chi_i \rho z) \cong 1$

and equation (3) becomes the following equation when integrated from 0 to ρt, where t is the specimen thickness:

$$I_i = \left(\frac{\Omega}{4\pi}\right)\frac{i\tau}{e}\,Q_i\,\omega_i\,\alpha_i(1+T_{CK,i})\,\varepsilon_i\,\frac{c_i}{A_i}\,N_0\,\rho t \qquad (5)$$

for normal electron incidence. This equation also assumes that the beam spreading and energy loss are negligible.

It is clear that the accuracy of the computation of absolute X-ray intensities with equations (2) and (3) [or equation (5) in the case of a thin film] depends on the accuracy of the many parameters used in these equations. These are now reviewed.

Fundamental Parameters for X-Ray Generation

In all of the parameters given in equation (2), the most important is the ionization cross section of the atomic shell from which the characteristic line of element i, Q_i originates. The probability of ionizing the atomic shell is proportional to the cross section. The best known equation to compute Q_i is the Bethe equation (Powell, 1976):

$$Q_i = 6.51\times10^{-20}\,\frac{Z_{nl}\,b_{nl}}{E_{nl,i}^2\,U}\ln(c_{nl}\,U)\ (\mathrm{cm}^2), \qquad (6)$$

where $E_{nl,i}$ is the ionization energy of the nl shell of element i, Z_{nl} is the number of electrons of that shell, and b_{nl} and c_{nl} are constants that depend on that shell. U is the overvoltage and is defined as $E_0/E_{nl,i}$. Powell (1976) suggested values of b_{nl} and c_{nl} from the experimental data available at that time, and he also showed (using a Fano plot that is $Q_i\,E_{nl,i}^2\,U$ as a function of $\ln U$ where the intercept and the slope of the straight line permits determination of b_{nl} and c_{nl}) that equation (5) is valid for $4 \le U \le 25$. The failure of equation (6) for $U \le 4$ is due to the fact that the Bethe equation was developed using the First Born approximation, which is not valid at low overvoltage. The failure for $U \ge 25$ is because equation (6) does not account for relativistic effects for the low and medium atomic numbers that were analyzed. In fact, the upper limit of this equation must be defined for $E_0 \le 30$ keV because relativistic effects depend on the energy of the incident electron, not on the overvoltage. The relativistic version of the Bethe equation is (Zaluzec, 1984):

$$Q_i = 6.51\times10^{-20}\,\frac{Z_{nl}\,b_{nl}}{E_{nl,i}\,E_r}\times\left\{\ln\left(\frac{c_{nl}\,E_r}{E_{nl,i}}\right)-\ln(1-\beta^2)-\beta^2\right\}(\mathrm{cm}^2), \qquad (7)$$

where $\beta = v/c$, the ratio of the speed of the electron to the speed of light, and $E_r = m_0 v^2/2$, where m_0 is the mass of the electron at rest.

However, values of the c_{nl} parameters obtained through Fano analysis from experimental data are generally smaller than one, giving negative values of the cross sections for $U \le 1/c_{nl}$ (for the nonrelativistic case). As a result of this limitation, Casnati et al. (1982) developed a semiempirical equation to compute ionization cross sections for K-shells, which includes a relativistic correction. This equation was found to be the most accurate to compute ionization cross sections by Gauvin (1993) and also by many others researchers. The Casnati et al. (1982) equation was used successfully to compute. EDS X-ray spectra of homogeneous Cu-Au and Ag-Au samples with K, L, and M lines by Gauvin et al. (2006) using the Monte Carlo program Win X-Ray. This was possible by using adjustment factors for the absolute values of the ionization cross sections in equation (2) but without including the Coster-Kronig factors. As a result, there is a large consensus in the X-ray microanalysis community that the Casnati equation is the best to compute ionization cross sections.

This consensus was obtained with a limited set of experimental data of good quality because the direct measurement of Q_i is difficult because of the cumulative errors of the many terms present in equation (2). Also, the theoretical computation of the ionization cross sections is fairly difficult because complex numerical methods are involved. Recently, Bote and Salvat (2008) succeeded in computing the ionization cross sections up to 1 GeV for all the elements from hydrogen ($Z = 1$) to einsteinium ($Z = 99$) using the relativistic plane-wave Born approximation (PWBA) with a semirelativistic version of the distorted-wave Born approximation (DWBA). These numerical computations were performed for the K, L_1, L_2, L_3, M_1, M_2, M_3, M_4, and M_5 shells and they were fitted to numerical equations that were published by Bote et al. (2009). For $U < 16$:

$$Q_i = 4\pi a_0^2\,\frac{U-1}{U^2}\left(a_1 + a_2\,U + \frac{a_3}{1+U} + \frac{a_4}{(1+U)^3} + \frac{a_5}{(1+U)^5}\right)^2; \qquad (8)$$

and for $U \ge 16$:

$$Q_i = 4\pi a_0^2\,\frac{U}{U+b}\,\frac{A_{nl}}{\beta^2}\left\{[\ln X^2 - \beta^2]\left(1+\frac{g_1}{X}\right) + g_2 + g_3(1-\beta^2)^{1/4} + \frac{g_4}{X}\right\}, \qquad (9)$$

where a_0 is the Bohr radius, β the ratio of the speed of the electron to that of light, and X is given by this equation:

$$X = \frac{\sqrt{E_0 + (E_0 + 2m_0c^2)}}{m_0 c^2}. \qquad (10)$$

In this last equation, m_0c^2 is the energy of the electron at rest, equal to 511 keV. The various a_i and g_i as well as b and A_{nl} are fitting parameters that depend on the atomic number of the atom as well as on the shell ionized, and they are tabulated in Bote et al. (2009).

Figures 2 and 3 show the ionization cross sections for the K-shells of C and Cu, respectively, as a function of E_0, measured experimentally by many researchers and also computed with the Bethe equation [equation (6)], the relativistic Bethe equation [equation (7)], the Casnati equation (Cas-

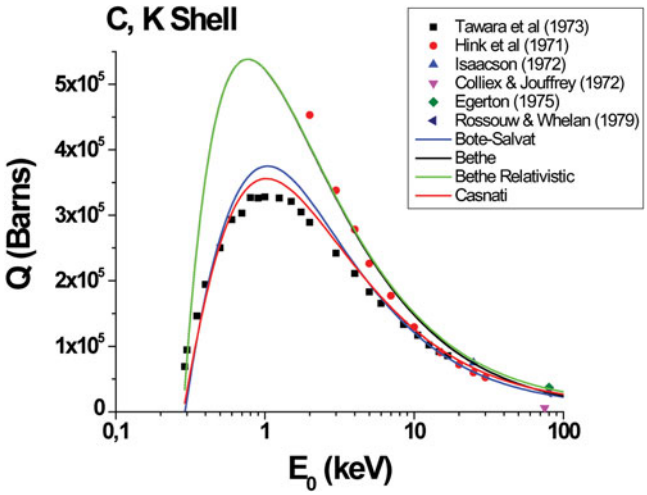

Figure 2. Ionization cross section for the K shell of C as a function of E_0 measured experimentally by many researchers and computed with the Bethe equation [equation (6)], the relativistic Bethe equation [equation (7)], the Casnati equation (Casnati et al., 1982), and the Bote-Salvat equation [equations (8)–(10)].

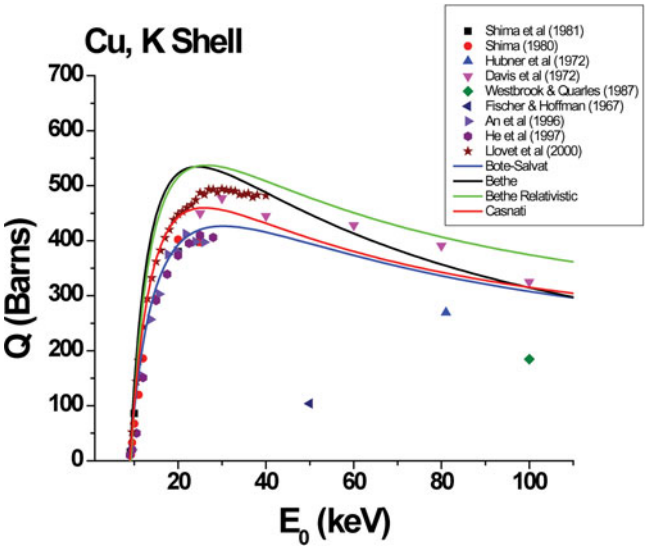

Figure 3. Ionization cross section for the K shell of Cu as a function of E_0 measured experimentally by many researchers and computed with the Bethe equation [equation (6)], the relativistic Bethe equation [equation (7)], the Casnati equation (Casnati et al., 1982), and the Bote-Salvat equation [equations (8)–(10)].

nati et al., 1982), and the Bote-Salvat equation [equations (8)–(10)]. In these figures, the units of cross section are barns (1 barn $= 1 \times 10^{-24}$ cm^2). The Bethe cross sections were computed with $b_{nl} = 0.9$ (Powell, 1976) and $c_{nl} = 1$. The most striking thing to notice is the strong scatter of the experimental values among different researchers, 25% for Cu and around 50% for C. This is not surprising because the measurement of Q_i is based on equation (5) where at least nine terms $(\Omega/4\pi, i, \tau, \omega_i, \alpha_i, T_{CK,i}, \varepsilon_i, C_i, \rho, t)$ must be known with high accuracy for precise determination. Since the variance of the statistical errors of the terms in equation (5) is additive, an error of 10% on each terms will lead to a minimum accuracy of 30% on the measured value of Q_i. A precision of 2.8% is therefore needed on these parameters to measure Q_i with accuracy of 5%, and this is a very difficult requirement to achieve in practice. The Bethe model for Q_i gives obviously too high values for $U < 4$, as a result of the failure of the first Born approximation, as mentioned above. Only at high electron energy (30 keV) does the relativistic Bethe equation start giving higher values of Q_i. The Casnati et al. (1982) and the Bote and Salvat (2008) equations give more realistic values of Q_i at low overvoltage, but they show significant differences. However, because of the uncertainties in the measured values of Q_i, in the order of 30%, it is not possible to determine which parameterization of the ionization cross sections is the most accurate.

For the parameters of equation (5), $(\Omega/4\pi)$ and ε_i depend on the EDS system and their values quoted by the manufacturer are the nominal values. The precise value of $(\Omega/4\pi)$ depends on the distance from the point of beam impact on the specimen to the center of the EDS crystal, the diameter of the crystal, and also that of the collimator. Without a precise knowledge of these values, the error introduced by using the nominal value could be significant. $(\Omega/4\pi)$ can be determined experimentally with calibrated nuclear sources but the uncertainty of the emitted X-ray intensity is around 10%. Alvisi et al. (2006) have shown that the relative difference between nominal and experimentally determined values of ε_i can be greater than 100% for the K_α line of carbon. The reason for this discrepancy is that the manufacturers are giving nominal values for the thicknesses of the various windows in front of the detector and also for the thickness of the active crystal that detects the X-rays. The manufacturers should determine the true thickness of their various windows or measure it experimentally with the method of Alvisi et al. (2006). It is clear that this lack of knowledge of the detector efficiency is a serious problem for the development of accurate quantitative standardless X-ray microanalysis and also that it affects the accuracy of the measured ionization cross sections.

In equation (5), i and τ can be determined with good accuracy if it is possible to measure the probe current in a given microscope with a Faraday cup. However, the value of the specimen density ρ for a thin film can have uncertainties depending on the preparation process. Also, the exact value of the specimen thickness could be difficult to measure with great accuracy. Electron energy loss spectroscopy (EELS) is now becoming a robust method to determine that, but its accuracy is of the order of 10% (Egerton, 2011), especially because of the uncertainties in the inelastic mean free path.

The accuracy of the fluorescence yield, ω_i, was estimated to be of the order of 5% for the K lines by Joy (2001). For the L lines, a survey of the compilation performed by Joy (2001) shows variations in the experimental data that fluctuate between 50 and 75%. However, another review by Campbell (2003) shows that the uncertainty for ω_{L3} and ω_{L2} is of the order of 5% while for ω_{L1} it is between 10 and 30%.

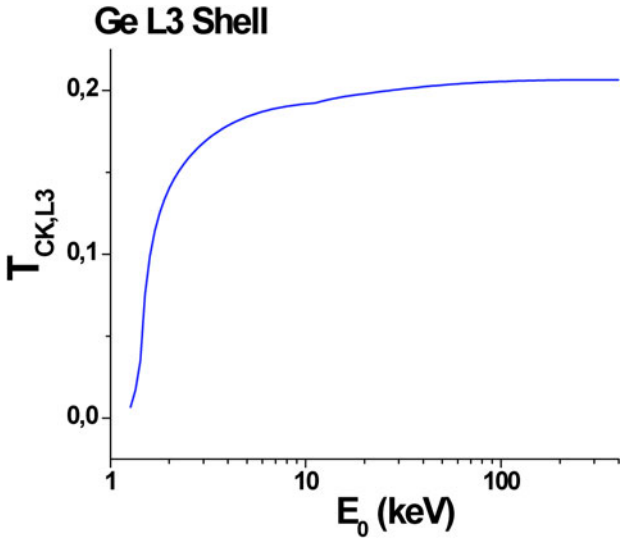

Figure 4. $T_{CK,L3}$ computed as a function of the beam energy, E_0, for Ge. See the text for details.

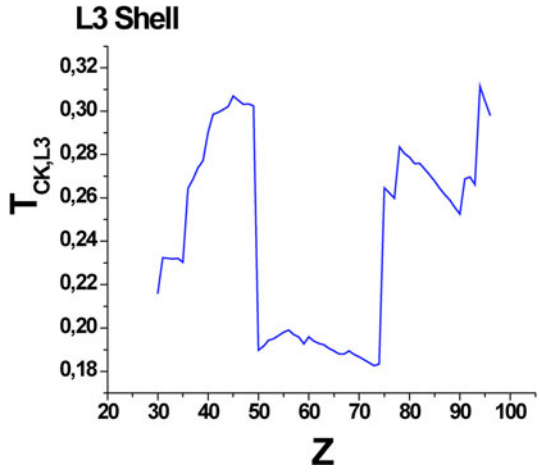

Figure 5. $T_{CK,L3}$ computed as a function of the atomic number Z. See the text for details.

Since there have been few measurements performed for the M lines, it is difficult to imagine that the accuracy will be better than that of the L lines. The accuracy of the weight of the characteristic line, α_i, was evaluated recently by Pia et al. (2009). From their compilation, it is seen that the experimental data fluctuate around 30% for the K-L_2 transition. For the L_1-M_2 transition, the fluctuation is around 60%. No data are reported for the M lines, and, again, it is difficult to forecast accuracy better than that of the L lines.

As shown by Merlet et al. (2004), the $(1 + T_{CK,i})$ factor accounts for nondirect ionization for vacancies in the L_i or M_i subshells. For an L_i subshell, vacancies are produced not only by direct ionization, but also by radiative and nonradiative transitions to the K shell, Coster-Kronig transitions between L_i subshells and by radiative transitions between L_i subshells. Since the ionization of the K shell can only be by direct electron impact, $T_{CK,i} = 0$ for the K lines. For the L_3 shell,

$$T_{CK,L3} = n_{KL3}\frac{Q_K}{Q_{L_3}} + f_{23}\frac{Q_{L_2}}{Q_{L_3}} + (f_{13} + f_{12}f_{13} + f'_{13})\frac{Q_{L_1}}{Q_{L_3}}, \tag{11}$$

where n_{KL3} is the radiative plus nonradiative yield for transitions of vacancies from the K shell to the L_3 subshell; f_{13}, f_{12}, and f_{13} are the Coster-Kronig yields between L subshells; and f'_{13} is the intrashell radiative yield for transitions of vacancies from the L_1 subshell to the L_3 subshell. It is clear that the $(1 + T_{CK,L3})$ parameter depends in a complicated way on the direct ionization cross sections of the L and the K shells weighted by the numerous parameters of equation (11). Figure 4 shows $T_{CK,L3}$ computed as a function of E_0 for Ge with the ionization cross sections of the three L shells of Bote and Salvat (2008) and the other parameters given by Merlet et al. (2004). Clearly, $T_{CK,L3}$ increases with E_0 and becomes almost constant for $U \geq 20 - 30$, where the ratios $Q_K/Q_{L_3}, Q_{L_1}/Q_{L_3}$ and Q_{L_2}/Q_{L_3} become also nearly constants.

Figure 5 shows $T_{CK,L3}$ computed as a function of the atomic number Z with the Coster-Kronig yields given by Campbell (2003), and assuming that n_{KL3} and f'_{13} are negligible and also that Q_{L1}/Q_{L3} and Q_{L2}/Q_{L3} are equal to 0.3 and 0.5 (based on the computations of Bote and Salvat, 2008). This factor fluctuates strongly as a function of Z and increases the generation of X-rays, for the L lines, by 20 to 30%. Assuming uncertainties of 10% on all the terms of equation (9), the uncertainty of $T_{CK,L3}$ is about 35%. Since $T_{CK,L3}$ depends on 10 parameters, all of them need to be known with very good accuracy too, but this is not the case so far and their precise determination is urgently needed for accurate quantitative X-ray microanalysis involving L lines (the same being true for M lines). A new method to measure the $(1 + T_{CK,i})$ factor is presented later in this article. Also, the uncertainties in the various values of equation (11) make the comparison between computed ionization cross sections and measured ones subjective because they depend on the choice of the specific factors of this equation.

This fact has to be kept in mind when the comparison of the ionization cross section of the Ge L_3 shell is made between the values computed by the Bethe equation [equation (6)], the relativistic Bethe equation [equation (7)], the Casnati equation (Casnati et al., 1982), and the Bote-Salvat equation [equations (8–10)], and those measured by Merlet et al. (2004), as shown in Figure 6. The Bethe cross sections were computed with $b_{nl} = 0.75$ (Powell, 1976) and $c_{nl} = 1$. Clearly, the Bote-Salvat cross sections are the closest to the experimental values, but this good agreement might be fortuitous due to the uncertainties in the many parameters of equation (11) and also on the experimental measurements of the ionization cross sections.

For the M lines, measurements of ionization cross sections were made by Merlet et al. (2008) for Au and Bi. In this case, the $T_{CK,M5}$ parameter is given by an equation more complicated than equation (11), and the associated parameters are less well known than for the L lines. However, they

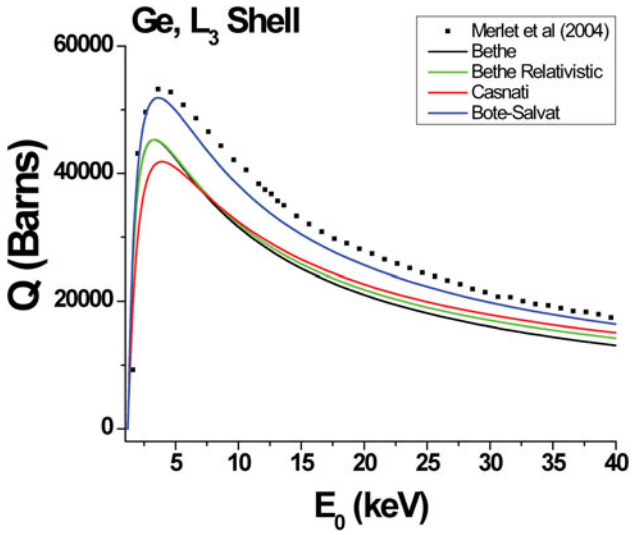

Figure 6. Comparison of the ionization cross section of the Ge L_3 between those computed by the Bethe equation [equation (6)], the relativistic Bethe equation [equation (7)], the Casnati equation (Casnati et al., 1982), and the Bote-Salvat equation [equations (7)–(9)], and those measured by Merlet et al. (2004).

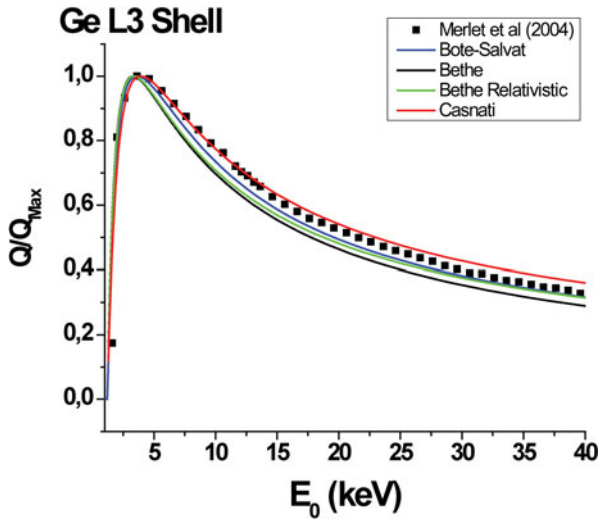

Figure 7. Comparison of the normalized values of the ionization cross section of the Ge L_3 to their maximum value between those computed by the Bethe equation [equation (6)], the relativistic Bethe equation [equation (7)], the Casnati equation (Casnati et al., 1982), and the Bote-Salvat equation [equations (7)–(9)] and those measured by Merlet et al. (2004).

found very good agreement with the values computed by Bote and Salvat (2008), but again this good agreement might be related to the choice of the parameters involved in the computation of $T_{CK,M5}$.

Figure 7 shows the comparison of the normalized values of the ionization cross sections of Figure 6. Clearly, the Casnati equation fits very well the experimental shape at low electron energy, and the Bote-Salvat fits very well the experimental shape at high electron energy. However, the relativistic Bethe curve is slightly lower than the Bote-Salvat at low electron energy (low overvoltage) and it is, again, a demonstration of the failure of the first Born approximation. As usual, the nonrelativistic Bethe equation gives too low values at high electron energy. Assuming that the experimental shape of Merlet et al. (2004) is good, none of these equations fits perfectly the shape of the ionization cross sections for the Ge L_3 shell. It is dangerous to generalize this result for all the shells and elements because of the limited set of experimental data. It has to be kept in mind that when a $\varphi(\rho z)$ curve is computed, only the relative shape of the cross section as a function of electron beam energy is needed.

Since the agreement between the absolute values of the measured ionization cross sections and those computed by Bote and Salvat (2008) seems to be the best so far, and also because they used a very consistent theory to compute them for all the elements from hydrogen ($Z = 1$) to einsteinium ($Z = 99$) up to 1 GeV for the K, L_1, L_2, L_3, M_1, M_2, M_3, M_4, and M_5 shells, these should be used to perform quantitative X-ray microanalysis, even if more measurements are urgently needed for the ionization cross sections and also for all the parameters presented in this section. Also, from this review on the fundamental parameters of X-ray generation, it is clear that accuracies in the measured ionization cross sections below 30% will be very difficult to achieve because of the error propagation of the many terms involved in equation (5).

Quantitative X-Ray Microanalysis in the Transmission Electron Microscope

Since it is difficult to determine accurately the specimen thickness in the TEM and also since probe current measurement is generally not a routine task, quantitative X-ray microanalysis is based on the ratio of the net intensities of two characteristic lines obtained in the same spectrum. In looking at equation (5), it is easy to see that in this ratio the probe current and the specimen thickness cancel out. However, knowledge of the specimen thickness is needed if absorption and fluorescence effects are not negligible. The ratio of the composition, c_A and c_B of two elements A and B, is related to the net X-ray intensity of their characteristic lines, I_A and I_B, although this equation neglects absorption and fluorescence (Cliff & Lorimer, 1975):

$$\frac{c_A}{c_B} = K_{A\text{-}B}\frac{I_A}{I_B}, \tag{12}$$

where $K_{A\text{-}B}$ is the famous Cliff and Lorimer K-factor. Looking at equation (5), it is easy to see that

$$K_{A\text{-}B} = \frac{Q_B\omega_B\alpha_B(1 + T_{CK,i})_B\varepsilon_B A_A}{Q_A\omega_A\alpha_A(1 + T_{CK,i})_A\varepsilon_A A_B}. \tag{13}$$

Equation (13) was first derived by Goldstein et al. (1977) without the use of the $(1 + T_{CK,i})$ factor because they were using, implicitly, an effective ionization cross section $Q_i^{eff} = Q_i(1 + T_{CK,i})$ for the L and M lines. Writing the $(1 + T_{CK,i})$

factor directly in equation (13) is preferable because it is a reminder of the importance of knowing with good accuracy the Coster-Kronig transitions factors for the use of this equation. Because of the uncertainties in the parameters in equation (13), the best accuracy for quantitative X-ray microanalysis in the TEM is obtained when the $K_{A\text{-}B}$ factors are determined experimentally with equation (12) using specimens of known composition for elements A and B and by measuring experimentally their net X-ray intensities I_A and I_B, as shown by Wood et al. (1984). When one of the two lines is outside the range where the detector efficiency is significantly smaller than 1, the $K_{A\text{-}B}$ factor becomes microscope dependent because each EDS detector has a different detection efficiency. Since it might be difficult to find a specimen of homogeneous composition for a given pair of elements A and B, the experimental determination of a $K_{A\text{-}B}$ factor relies on interpolating its value from measured values $K_{A\text{-}C}$ and $K_{B\text{-}C}$ using $K_{A\text{-}B} = K_{A\text{-}C}/K_{B\text{-}C}$, as can be easily seen with equation (13). However, the experimental measurement of the $K_{A\text{-}B}$ factors is a disadvantage because it takes time to find or to make an alloy or a compound, assess its homogeneity, and determine its composition with an accuracy below 5% (if not 2%) using another quantitative method. Fabricating a thin foil is not generally a straightforward task and many EDS spectra must be measured. Things are even more complicated if a $K_{A\text{-}B}$ factor is interpolated from two others determined experimentally. As a result, most of the quantitative work is performed with computed $K_{A\text{-}B}$ factors using equation (13), despite all the uncertainties in it as shown previously.

It is often said, or thought, that the Cliff and Lorimer method is only valid for specimens thin enough to avoid X-ray absorption and fluorescence. This is, of course, wrong because absorption and fluorescence corrections do exist for thin films having a given thickness. By neglecting f_{Br} and f_{ind} in equation (2), equation (12) can be rewritten as follows:

$$\frac{c_A}{c_B} = K_{A\text{-}B} A_{A\text{-}B} F_{A\text{-}B} \frac{I_A}{I_B}. \tag{14}$$

$A_{A\text{-}B}$ is the absorption correction, given by

$$A_{A\text{-}B} = \frac{\int_0^t \varphi(\rho z)_B e^{-\chi_B \rho z}\, d\rho z}{\int_0^t \varphi(\rho z)_A e^{-\chi_A \rho z}\, d\rho z} \tag{15}$$

and if the specimen thickness is small enough, for a given incident electron energy to avoid beam spreading, energy loss, and electron backscattering, $\varphi(\rho z)_B \cong \varphi(\rho z)_A \cong 1$ then equation (15) gives

$$A_{A\text{-}B} = \frac{\chi_A[1 - e^{-\chi_B \rho t}]}{\chi_B[1 - e^{-\chi_A \rho t}]}. \tag{16}$$

This is the famous equation derived by Goldstein et al. (1977) to correct for X-ray absorption in the TEM. The equation applies only for thin specimens with parallel surfaces, as described above, having the same composition and thickness in a distance perpendicular to the incident beam and in the direction of the X-ray detector, equal to $t/\tan\psi$, where ψ is the take-off angle. In equation (14), $F_{A\text{-}B}$ is given by

$$F_{A\text{-}B} = \frac{\left(1 + \sum_{j=1}^{n} f_{c,j}\right)_B}{\left(1 + \sum_{j=1}^{n} f_{c,j}\right)_A}, \tag{17}$$

where the summation for each element (A and B) is taken for the n characteristic lines present in the spectrum, having an energy greater than the characteristic line of element A or B. Nockolds et al. (1980) derived an absorption correction for thin films of uniform thickness when the line B fluoresces A (or the line A fluoresces B). Anderson et al. (1995) have developed formulas for fluorescence corrections involving more complex geometries. The Cliff and Lorimer method assumes that the sum of the mass fraction of all the elements equals 1. Putting this constraint for a binary system in equation (14) and by noting that $A_{A\text{-}B} = \gamma_B/\gamma_A$, we obtain

$$c_A = \frac{1}{1 + K_{B\text{-}A} \dfrac{\gamma_A}{\gamma_B} F_{B\text{-}A} \dfrac{I_B}{I_A}}, \tag{18}$$

where $K_{B\text{-}A} = 1/K_{A\text{-}B}$ and $F_{B\text{-}A} = 1/F_{A\text{-}B}$. When absorption and/or fluorescence are significant, this equation needs to be iterated until convergence is obtained in the value of c_A because the mass absorption coefficients, used in these corrections, are composition dependent as seen in equation (4). When absorption, fluorescence, and δ_{ind} are negligible, equation (18) can be solved directly for a binary system.

Generally, due to the small thickness of films used in the TEM, the fluorescence correction is negligible and the absorption correction is significant only for X-ray lines having an energy below 1 keV because their mass absorption coefficients have very high values (in the range of 10^4 to 10^5 cm^2/g). However, with focused ion beam specimens, bulk regions surround thin films and fluorescence effects are likely to be significant; the microanalyst should be aware of this and more research is needed to quantify this effect. Also, the accuracy of mass absorption coefficients with photon energy between 0.5 to 1 keV is in the range of 10% to 20% and 100% to 200% for photon energy between 0.1 to 0.5 keV (Hubbell, 1999), and this limits the accuracy of absorption correction. Finally, the application of the absorption and the fluorescence corrections relies on the knowledge of the specimen thickness at the point of analysis, which might be difficult to determine at that point. It is for that reason that Watanabe and Williams (2006) developed the ζ factor method that relies on the measurement of the probe current with a Faraday cup and the experimental determination of several ζ factors with specimens of known composition and thickness. The measurement of the probe

current then permits precise determination of the thickness of the analyzed regions, and the absorption and fluorescence corrections can be computed to determine the composition of materials with improved accuracy. However, most microscopes do not accommodate routine measurement of the probe current, and the conventional Cliff-Lorimer method is still being used extensively. A method to determine the specimen thickness with bright-field–dark-field imaging is proposed below.

Quantitative X-Ray Microanalysis in the Scanning Electron Microscope

As explained in the introduction of this article, quantitative X-ray microanalysis in the SEM and in the electron microprobe is performed using the ZAF method. By inserting equation (5) into equation (1) and neglecting δ_{ind}, we obtain

$$\frac{c_i}{c_{(i)}} = \frac{\gamma_{(i)}\left(1 + \left\{\sum_{j=1}^{m} f_{c,j}\right\} + f_{Br}\right)_{(i)}}{\gamma_i\left(1 + \left\{\sum_{j=1}^{m} f_{c,j}\right\} + f_{Br}\right)_i} \frac{I_i}{I_{(i)}}. \qquad (19)$$

The atomic number correction, Z_i, is (Horny et al., 2010)

$$Z_i = \frac{\int_0^\infty \varphi(\rho z)_i \, d\rho z}{\int_0^\infty \varphi(\rho z)_{(i)} \, d\rho z}. \qquad (20)$$

The absorption correction is given by (Castaing, 1951)

$$A_i = \frac{f(\chi_{(i)})}{f(\chi_i)}, \qquad (21)$$

where

$$f(\chi_i) = \frac{\int_0^\infty \varphi(\rho z)_i \, e^{-\chi_i \rho z} \, d\rho z}{\int_0^\infty \varphi(\rho z)_i \, d\rho z} \qquad (22)$$

and a similar expression exists for $f(\chi_{(i)})$. $f(\chi_i)$ is the ratio of the emitted X-rays to the generated X-rays of the characteristic line of element i in the analyzed specimen and $f(\chi_{(i)})$ is the same, for the standard. The fluorescence correction factor is therefore

$$F_i = \frac{\left(1 + \left\{\sum_{j=1}^{m} f_{c,j}\right\} + f_{Br}\right)_{(i)}}{\left(1 + \left\{\sum_{j=1}^{m} f_{c,j}\right\} + f_{Br}\right)_i}. \qquad (23)$$

On looking at the equations (1) and (19)–(23), it is clear that the Z_i and A_i corrections are related to each other since $\gamma_{(i)}/\gamma_i = Z_i A_i$. It is worth mentioning that $Z_i A_i F_i$ could be rewritten as $E_i F_i$ with $E_i = \gamma_{(i)}/\gamma_i$, E_i being the ratio of emitted X-ray intensity of the standard of known composition to that of the specimen of unknown composition for the characteristic line of element i. The only reason that $Z_i A_i$ is used instead of E_i is historical, the A_i corrections being introduced by Castaing (1951) before Duncumb (1957) discovered the Z_i correction.

Z_i and A_i are the dominant terms in the ZAF correction because fluorescence effects are often negligible. In looking at equation (18), the genius of Castaing is clear. The ratio of the net intensity of a characteristic line measured in the specimen of unknown composition to that of the standard of known composition, for the same X-ray lines of each element i, removes all these parameters—the ionization cross section, the fluorescence yield, the weight of the characteristic line, the Coster-Kronig transition factor, and the detector efficiency. Therefore, their precise knowledge is not needed and their inaccuracies cannot affect the accuracy of the quantification. The validity of equation (19) relies on the use of the same experimental parameters to measure the intensities of the specimen of unknown and the standards of known composition—the same solid angle, probe current, acquisition time, and take off angle. Only a good shape of the $\varphi(\rho z)$ curve is needed in addition to accurate mass absorption coefficients when the absorption correction is significant.

The best $\varphi(\rho z)$ models, giving the $Z_i A_i$ corrections, are those that were proposed by Pouchou and Pichoir (1984), Merlet (1994), and Bastin et al. (1998). For the fluorescence correction, when the standard is a pure element, $f_{c,j}$ is null. For a multielement specimen, an expression for the characteristic fluorescence, $f_{c,j}$, was developed by Reed (1965), and Henoc (1968) developed an expression for the bremsstrahlung fluorescence, f_{Br}. Accuracy as good as 1% can be obtained in the electron microprobe, and this is the most accurate quantitative method for chemical analysis. However, this accuracy is obtained with careful measurements of X-ray intensities for the specimen of unknown composition, and the standards and the bulk specimen must be flat and should have a homogeneous composition.

The *f*-Ratio Method

The *f*-ratio method was developed by Horny et al. (2010) as an alternative to the conventional ZAF method in situations when the measurement of the probe current is difficult (there is no Faraday cup installed in the electron microscope to measure the probe current) or for microscopes that do not have a very stable probe current, as in cold-field electron emitters. This method extends the idea developed by Cliff and Lorimer (1975) of using an intensity ratio to eliminate the need to know the probe current. However, in the Cliff and Lorimer method, when the intensity I_B of the element B is close to 0, the ratio I_A/I_B increases rapidly and tends to diverge and because I_B is small, the ratio then becomes dominated by the noise. Horny et al. (2010) have proposed the *f*-ratio to avoid this problem. The ratio f_A is defined as

$$f_A = \frac{I_A}{I_A + I_B}. \tag{24}$$

The *f*-ratio is normalized between 0 and 1. The Horny et al. (2010) new method was developed for a binary system, A and B, but it can be extended to multielement systems.

By inserting equation (24) in equation (2), neglecting f_{ind} and assuming that $c_A + c_B = 1$ (as in the Cliff and Lorimer method), Horny et al. (2010) obtained

$$f_A = \frac{1}{1 + K_{A\text{-}B}\dfrac{\gamma_B\left(1 + \sum_{j=1}^{m} f_{c,j} + f_{Br}\right)_B}{\gamma_A\left(1 + \sum_{j=1}^{m} f_{c,j} + f_{Br}\right)_A}\dfrac{(1 - c_A)}{c_A}}. \tag{25}$$

In this article, the composition of the NIST SRM-482 Cu-Au standard for the three compositions of 20, 60, and 80% Cu was determined with an accuracy around 5% using calibration curves relating f_A as a function of c_A, as shown in Figure 1a. Monte Carlo simulations were used to determine the calibration curves. Because of the uncertainties in the computation of the $K_{\text{Cu-Au}}$ factor, a calibration factor was determined for all the electron beam energies used. The alloy having a composition of 40% was used for that purpose. Clearly, this is a disadvantage because finding an alloy (or a compound) of known and homogeneous composition might be impossible for a given system A-B. Also, having to measure the calibration factor every time the beam energy is varied can be time-consuming. This fact will become more important as methods for the characterization of materials based on the uses of different beam energies are being more and more used. A method to calibrate the $K_{A\text{-}B}$ factor at only one beam energy is therefore needed because true standardless X-ray microanalysis with an accuracy better than 5% is not possible now. This will be discussed more rigorously in the next section of this article.

By comparing equations (25) and (19), it should be clear that the Cliff and Lorimer factor, $K_{A\text{-}B}$, appears naturally in any quantitative X-ray microanalysis method involving the ratio of two different lines taken on the same spectrum, both for thin foils and for bulk specimens. Of course, the correction factors for the generation, absorption, fluorescence, and other indirect X-ray generation are different and depend on the geometry and on the distribution of the various phases of the specimen.

By defining $G_{B\text{-}A}$ as

$$G_{B\text{-}A} = \Lambda_{A\text{-}B}\, K_{A\text{-}B}\, \frac{\gamma_B}{\gamma_A}\, \frac{\left(1 + \sum_{j=1}^{m} f_{c,j} + f_{Br} + f_{ind}\right)_B}{\left(1 + \sum_{j=1}^{m} f_{c,j} + f_{Br} + f_{ind}\right)_A}, \tag{26}$$

where $\Lambda_{A\text{-}B}$ is the experimental calibration factor of the Cliff and Lorimer factor (see Horny et al., 2010 for details about its determination), equation (24) can be solved as follows:

$$c_A = \frac{f_A\, G_{B\text{-}A}}{1 + f_A(G_{B\text{-}A} - 1)} \tag{27}$$

and when the corrections factors for the generation, absorption, fluorescence, and other indirect X-ray generation are significant, this equation must be solved iteratively. When absorption, fluorescence, and other indirect X-ray generation effects are negligible, $G_{B\text{-}A} = \Lambda_{A\text{-}B} K_{A\text{-}B}$ and equation (27) can be solved directly. It is interesting to note that when $G_{B\text{-}A} \cong 1$, $c_A \cong f_A$. Also, at the low concentration limit, $f_A \to 0$ and $c_A \cong G_{B\text{-}A} f_A$.

This method was extended to multielement systems by Gauvin et al. (to be submitted for publication[a]), and the full analysis of the error propagation in the quantification procedure was analyzed. This shows that the *f*-ratio has a smaller error than the I_A/I_B ratio, but the overall error is the same for both methods when the propagation of errors in the equations used to determine the composition are computed. However, since the *f*-ratio is less sensitive to noise propagation than the I_A/I_B ratio, qualitative chemical maps should be built based on this new ratio method.

Toward Standardless Quantitative X-Ray Microanalysis

The author of this article strongly believes that any standardless quantitative X-ray microanalysis method should be based on the ratio of net X-ray intensities acquired on the same spectrum and the *f*-ratio method is the natural choice. For that purpose, the Cliff and Lorimer factors need to be computed exactly. As mentioned many times in this article, this is not yet possible and, in this section, some ideas to help in this regard are presented. It should be clear to the reader that more research is needed to fully validate these new ideas.

Ratio of Cliff and Lorimer Factor Obtained at Two Different Accelerating Voltages

In his PhD thesis, Gauvin (1990) proposed using the ratio of a Cliff and Lorimer factor measured at two different accelerating voltages E_1 and E_2 for the same elements A and B, defined as

$$R_{A\text{-}B}^{E_2\text{-}E_1} = \frac{K_{A\text{-}B}^{E_2}}{K_{A\text{-}B}^{E_1}}, \tag{28}$$

where $E_2 > E_1$ by definition. Looking at equation (13), it is seen that the ionization cross sections and also the $(1 + T_{CK,i})$ factor for the L and M lines depend only on electron energy. For the $(1 + T_{CK,i})$ factor, this is when E_2 or E_1 are smaller than 20 to 30 times the ionization energy of

[a]Gauvin, R., Michaud, P., Demers, H. & Trudeau, M.L. The application of the *f*-ratio method for quantitative X-ray microanalysis in the transmission electron microscope. To be submitted for publication to *Microscopy & Microanalysis*.

elements A and/or B. Assuming that E_1 is sufficiently high to neglect the variation of the $(1 + T_{CK,i})$ factor for the L and M lines with electron beam energy, insertion of equation (13) in equation (28) gives

$$R_{A\text{-}B}^{E_2\text{-}E_1} = \frac{Q_B^{E_2} Q_A^{E_1}}{Q_A^{E_2} Q_B^{E_1}}. \tag{29}$$

Equation (29) is always true when only K lines are involved. By inserting the Bethe equation for Q_i [equation (6)] in equation (29), all the terms in front of the natural logarithm cancel out, giving

$$R_{A\text{-}B}^{E_2\text{-}E_1} = \frac{\ln(c_{nl} U_B^{E_2}) \ln(c_{nl} U_A^{E_1})}{\ln(c_{nl} U_A^{E_2}) \ln(c_{nl} U_B^{E_1})}. \tag{30}$$

Assuming that c_{nl} is not a function of the atomic number, Gauvin (1990) obtained this equation for its computation:

$$\ln(c_{nl}) = \sqrt{\frac{\psi^2}{4} - \frac{(R_{A\text{-}B}^{E_2\text{-}E_1} \alpha - \beta)}{R_{A\text{-}B}^{E_2\text{-}E_1} - 1}} - \frac{\psi}{2}, \tag{31}$$

where

$$\psi = \ln(U_B^{E_1} U_A^{E_2}) = \ln(U_B^{E_2} U_A^{E_1}) \tag{32}$$

$$\alpha = \ln(U_B^{E_1}) \ln(U_A^{E_2}) \tag{33}$$

$$\beta = \ln(U_B^{E_2}) \ln(U_A^{E_1}). \tag{34}$$

Gauvin (1990) also derived a similar equation for the c_{nl} parameter of the relativistic Bethe equation [equation (7)]. In addition he derived equations to compute the c_{nl} parameter of each element A and B with the use of two different $R_{A\text{-}B}^{E_2\text{-}E_1}$ factors to take into account the possible variation of the c_{nl} parameter with atomic number.

$R_{A\text{-}B}^{E_2\text{-}E_1}$ depends only on the ratio of the cross sections—all the others parameters disappear in this ratio. This is a great advantage because we have seen that the uncertainties in the fluorescent yield, ω_i, the weight of the characteristic line, α_i, the Coster-Kronig transitions, $(1 + T_{CK,i})$, and the detector efficiency, ε_i, are all greater than, at least, 10%. Since it is possible to measure Cliff and Lorimer factors with great accuracy, the $R_{A\text{-}B}^{E_2\text{-}E_1}$ factor can be determined with great accuracy. This is very important because what is needed to compute a $K_{A\text{-}B}$ factor for performing quantitative X-ray microanalysis is the ratio of cross sections Q_B/Q_A, not their absolute values Q_A and Q_B. The $R_{A\text{-}B}^{E_2\text{-}E_1}$ factor is a normalized ratio of Q_B/Q_A at a reference energy E_1. Therefore, by fixing E_1, the variation of $R_{A\text{-}B}^{E_2\text{-}E_1}$ gives the shape of Q_B/Q_A as a function of E_2, allowing comparison of the various models of cross section with accurate measured values of $R_{A\text{-}B}^{E_2\text{-}E_1}$. Using a good model of cross section to compute $R_{A\text{-}B}^{E_2\text{-}E_1}$ with equation (29), the experimental $K_{A\text{-}B}$ factor needs to be determined only at one electron beam energy E_1 and the factor at an electron beam energy E_2 can be accurately determined using equation (28) as follows:

$$K_{A\text{-}B}^{E_2} = R_{A\text{-}B}^{E_2\text{-}E_1} K_{A\text{-}B}^{E_1}. \tag{35}$$

Therefore, with an accurate knowledge of the $R_{A\text{-}B}^{E_2\text{-}E_1}$ ratio, it is only necessary to determine experimental Cliff and Lorimer factors at one electron beam energy, and this should help in the implementation of the *f*-ratio method presented previously.

Gauvin (1990) used the Cliff and Lorimer factors measured at 100 and 200 keV by Schreiber and Wims (1981) to determine the c_{nl} parameter of the nonrelativistic Bethe equation [equation (6)] using equations (30)–(34). Assuming that the b_{nl} parameter is not a function of the atomic number, as in the Powell (1976) parameterization, only the c_{nl} parameter is needed to compute the ratio of cross sections Q_B/Q_A in Cliff and Lorimer factors. Also, the use of the relativistic equation of Bethe [equation (7)] did not change the computed values of Q_B/Q_A. Excellent agreement was found between Cliff and Lorimer factors computed in this way with those measured by Gauvin (1990) and also with those measured by Wood et al. (1984). The comparison was performed for Cliff and Lorimer factors with the energy of their characteristic lines being between 5 and 15 keV where the detector efficiency was close to 1 with the EDS detectors used at that time. The article of Gauvin and L'Espérance (1991) gives the details about this work and also the derivations of the various equations to compute c_{nl}.

The $R_{A\text{-}B}^{E_2\text{-}E_1}$ ratio can also be used to compare measured values of ionization cross sections by computing it with two separate ratios $Q_B^{E_2}/Q_B^{E_1}$ and $Q_A^{E_1}/Q_A^{E_2}$ determined from two different experimental sets. Figure 8 shows $R_{\text{C-Cu}}^{E_0\text{-}E_1}$ as a function of E_0, with E_1 equal to 10 keV, computed with some of the experimental ionization cross sections of C and Cu shown in Figures 2 and 3 and with the model of Casnati et al. (1982) and with the computations of Bote and Salvat [equations (8)–(10)]. The ratio of the cross sections for carbon was obtained from a logarithmic fit of the values measured by Hink & Pashke (1971*a*, 1971*b*) and by Tawara et al. (1973). Two $R_{\text{C-Cu}}^{E_0\text{-}E_1}$ ratios were computed from the ratio of cross sections of copper measured by He et al. (1997) and by Llovet et al. (2000). Clearly, the $R_{\text{C-Cu}}^{E_0\text{-}E_1}$ ratio computed with Bote-Salvat cross sections is greater than that computed with Casnati cross sections for E_0 greater than 20 keV. Also, the $R_{\text{C-Cu}}^{E_0\text{-}E_1}$ ratio computed with Bote-Salvat cross sections is closer but significantly smaller than the experimental ratio computed with Llovet et al. (2000) Cu cross sections. The $R_{\text{C-Cu}}^{E_0\text{-}E_1}$ ratios obtained with the experimental Cu cross sections of He et al. (1997) are the farthest from the theoretical predictions. This is interesting because in Figure 3 it is seen that they are very close to the computed values of Bote-Salvat. This finding must be "taken with a grain of salt" because these experimental ratios were computed with sets of ionization cross sections that have differences around 30% for Cu and 60% for C, giving an estimated error on the $R_{\text{C-Cu}}^{E_0\text{-}E_1}$ ratio that is about 100%. This fact highlights that $R_{A\text{-}B}^{E_2\text{-}E_1}$ ratios should be obtained from the measurement of Cliff and Lorimer factors, or ratios of net X-ray intensities, at different values of beam energy, as will be explained in more detail below.

Looking at equation (31), the validity of equation (30) to compute $R_{A\text{-}B}^{E_2\text{-}E_1}$ can be demonstrated if a plot of $\sqrt{\psi^2/4 - ((R_{A\text{-}B}^{E_2\text{-}E_1} \alpha - \beta)/(R_{A\text{-}B}^{E_2\text{-}E_1} - 1))}$ as a function of ψ

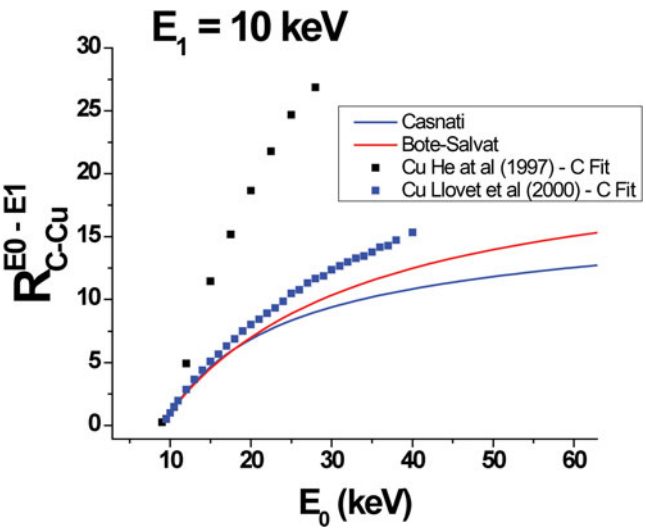

Figure 8. $R_{\text{C-Cu}}^{E_0\text{-}E_1}$ as a function of E_0 with E_1 equal to 10 keV, computed with some of the experimental ionization cross sections of C and Cu shown in Figures 2 and 3 and with the model of Casnati et al. (1982) and with the computations of Bote and Salvat [equations (8)–(10)]. See the text for details.

gives a straight line with a slope of 1/2 and the intercept at the origin being $\ln(c_{nl})$. Figure 9 shows $\sqrt{\psi^2/4 - ((R_{\text{A-B}}^{E_2\text{-}E_1}\alpha - \beta)/(R_{\text{A-B}}^{E_2\text{-}E_1} - 1))}$ as a function of ψ with $R_{\text{C-Cu}}^{E_0\text{-}E_1}$ computed from 10 to 400 keV with the ionization cross sections of Bethe [equation (6)], Bethe relativistic [equation (7)], Casnati et al. (1982), and Bote-Salvat [equations (8)–(10)], and Table 1 gives the values of the parameters of the linear fit of these plots performed by regression analysis. In all the cases, a straight line is obtained with a slope equal to 0.5 for Bethe, Bethe relativistic, Casnati, and 0.495 from the values of Bote-Salvat. The good agreement of the relativistic Bethe equation to compute $R_{\text{C-Cu}}^{E_0\text{-}E_1}$ with equation (30) was expected, but the excellent agreements of the Casnati et al. (1982) and Bote-Salvat ionization cross sections are absolutely astounding. This might suggest that slight modifications of the Bethe equations could be needed to account for the failure of the first Born approximation below four times the ionization energy of the shell of the ionized element.

For the Bote-Salvat cross sections, because the slope equals 0.495, equation (30) will not give good $R_{\text{C-Cu}}^{E_0\text{-}E_1}$ ratios with the determined value of c_{nl}. The determined value of the slope must be used and details in that regard are given in Appendix A.

Figure 10 shows $\sqrt{\psi^2/4 - ((R_{\text{A-B}}^{E_2\text{-}E_1}\alpha - \beta)/(R_{\text{A-B}}^{E_2\text{-}E_1} - 1))}$ as a function of ψ with the $R_{\text{C-Cu}}^{E_0\text{-}E_1}$ values shown in Figure 8 and Table 2 gives the values of the parameters of the linear fit of these plots performed by regression analysis. The different values of m and c_{nl} obtained here for the Casnati and Bote-Salvat cross sections are because the fit was performed between 10 and 50 keV, and more deviations are observed with the Bethe theory because the failure of the Born approximation below U equal to 4 will be more significant than seen previously. However, a straight line is

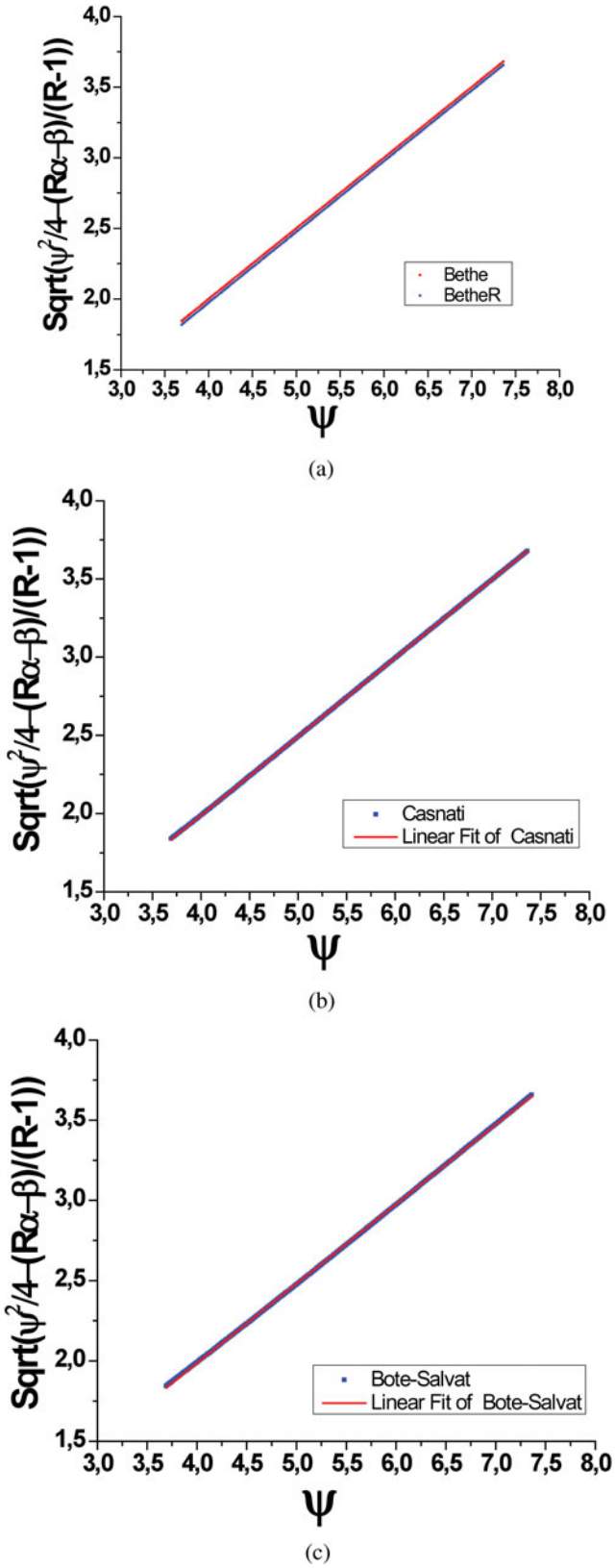

Figure 9. $\sqrt{\psi^2/4 - ((R_{\text{A-B}}^{E_2\text{-}E_1}\alpha - \beta)/(R_{\text{A-B}}^{E_2\text{-}E_1} - 1))}$ as a function of ψ, given by equations (31)–(34), with $R_{\text{C-Cu}}^{E_0\text{-}E_1}$ computed from 10 to 400 keV with the ionization cross sections of (**a**) Bethe [equation (6)] and Bethe relativistic [equation (7)], (**b**) Casnati et al. (1982), and (c) Bote-Salvat [equations (8)–(10)].

Table 1. Values of the Parameters of the Linear Fit of Equation (30) with $R^{E_0\text{-}E_1}_{\text{C-Cu}}$ Computed from 10 to 400 keV with the Ionization Cross Sections of Bethe [equation (6)], Bethe Relativistic [equation (7)], Casnati et al. (1982), and Bote-Salvat [equations (8)–(10)].*

Q Model	m	c_{nl}	R^2
Bethe	0.5 ± 2.42e−8	1 ± 1e−7	1
Bethe relativistic	0.50064 ± 1.58e−5	0.972 ± 1e−4	1
Casnati	0.502 ± 9e−5	0.98 ± 1e−4	0.99999
Bote-Salvat	0.495 ± 3e−4	1.007 ± 1e−3	0.99998

*The plots are shown in Figure 9.

Table 2. Values of the Parameters of the Linear Fit of Equation (31) Obtained with the $R^{E_0\text{-}E_1}_{\text{C-Cu}}$ Taken from Figure 8.*

Q	m	c_{nl}	R^2
He et al. (1997)	0.56 ± 0.03	0.8 ± 0.1	0.977
Llovet et al. (2000)	0.5199 ± 5e−4	1.06 ± 0.003	0.99997
Casnati	0.49941 ± 4e−4	0.993 ± 1e−3	0.99995
Bote-Salvat	0.483 ± 3e−4	1.06 ± 0.001	0.99997

*The plots are shown in Figure 10.

still observed for both models, which is again astounding. Also, the data obtained with the measurements of He et al. (1997) seem to be the worst. They deviate very significantly from exact Bethe behavior, and the quality of the fit is bad at low electron energy (low values of ψ). The fit of the measurements of Llovet et al. (2000) for Cu seems to give the best values, a beautiful line is observed with their data. However, it is difficult to draw definite conclusions because, as mentioned previously, the errors on the experimental $R^{E_0\text{-}E_1}_{\text{C-Cu}}$ ratios used here are around 100%. The results presented in the last two figures are intended to show how the analysis of $\sqrt{\psi^2/4 - ((R^{E_2\text{-}E_1}_{A\text{-}B}\,\alpha - \beta)/(R^{E_2\text{-}E_1}_{A\text{-}B} - 1))}$ as a function of ψ can be useful to assess the quality of models of ionization cross section to compute $R^{E_2\text{-}E_1}_{A\text{-}B}$ and also to access the quality of experimental data of ionization cross sections. To determine which model of ionization cross section should be used to compute $R^{E_2\text{-}E_1}_{A\text{-}B}$ ratios, precise measurements of $R^{E_2\text{-}E_1}_{A\text{-}B}$ are needed.

When using equation (12) to measure a $K_{A\text{-}B}$ factor, its accuracy is determined by the errors of the values of c_A, c_B, I_A, and I_B. The accuracy of the compositions depends on the experimental method that was used for their determination, and the best methods should give an accuracy of about 5%. The error on the net X-ray intensity is mainly the statistical noise coming from their emissions as is described by Poisson statistics, the statistical error, ε_{st}, on the measurement of the characteristic X-ray intensity of element i, I_i, being

$$\varepsilon_{st} = 300\,\frac{\sqrt{I_i}}{I_i}\ (\%) \tag{36}$$

at the 99% level of confidence. If 10,000 counts are obtained for I_A and I_B, each measured value of intensity will have a statistical error of 3%. Adding the errors in quadrature, the overall error on a $K_{A\text{-}B}$ factor measured with electron beam energy of E_1 is 8.25%. If the ratio $R^{E_2\text{-}E_1}_{A\text{-}B}$ is computed using two $K_{A\text{-}B}$ factors measured with the same accuracy, the overall accuracy of this ratio will be around 12%. This value above 10% is due to the propagation of the errors on the values of the composition and on the values of the net X-ray intensities. Not only the composition must be known accurately to measure a good $K_{A\text{-}B}$ factor, but most importantly a specimen of homogeneous composition must be found to measure it and, as mentioned previously, this might be impossible for a given system A-B. Also, if absorption is significant, the errors in the determination of the specimen thickness will propagate in the absorption correction and in the resulting $K_{A\text{-}B}$ factor.

Therefore, it might be advantageous to measure directly the $R^{E_2\text{-}E_1}_{A\text{-}B}$ ratio. If the two $K_{A\text{-}B}$ factors are measured for the same homogeneous specimen, the composition cancels out in the $R^{E_2\text{-}E_1}_{A\text{-}B}$ ratio and the insertion of equation (12) into equation (28) gives

$$R^{E_2\text{-}E_1}_{A\text{-}B} = \frac{I_B^{E_2} I_A^{E_1}}{I_A^{E_2} I_B^{E_1}}. \tag{37}$$

An accuracy better than 5% can be achieved if all four measured net X-ray intensities have at least 14,400 counts. If the measurements are performed in the same region of the specimen at the two energies E_1 and E_2, there is no need to know the composition of the specimen. Even better, if the specimen is thin enough, relative to the electron beam energy, equation (16) is applicable to compute the absorption correction, and it is the same at the two electron beam energies because the thickness of the specimen and the composition of the material where the X-ray propagates through the EDS detector are the same. Therefore, when the ratio I_B/I_A is measured in the same region (or very close to the same region) at the energies E_1 and E_2, not only there is no need to know the composition of the material to measure $R^{E_2\text{-}E_1}_{A\text{-}B}$, but the absorption correction cancels out if there is negligible beam spreading in the specimen. It will be possible to measure many $R^{E_2\text{-}E_1}_{A\text{-}B}$ ratios for many combinations of elements with very high accuracy, even for light elements when X-ray absorption is significant. In the case of significant absorption, particulates or films in the 5–50 nm range might have to be used depending on the electron beam energy, dictated by the absence of beam spreading in the material—the higher the beam energy, the greater the allowable thickness.

Determination of the Coster-Kronig Transitions Factor

Equation (29) is exact for the K lines and the minimum energy where it is valid for the L and M lines is above 20 to 30 times the ionization energy of the shell, as shown above. The introduction of the Coster-Kronig transition factors in the $R^{E_2\text{-}E_1}_{A\text{-}B}$ ratios for L and M lines can be seen as a limitation of the work presented so far. However, it is shown in

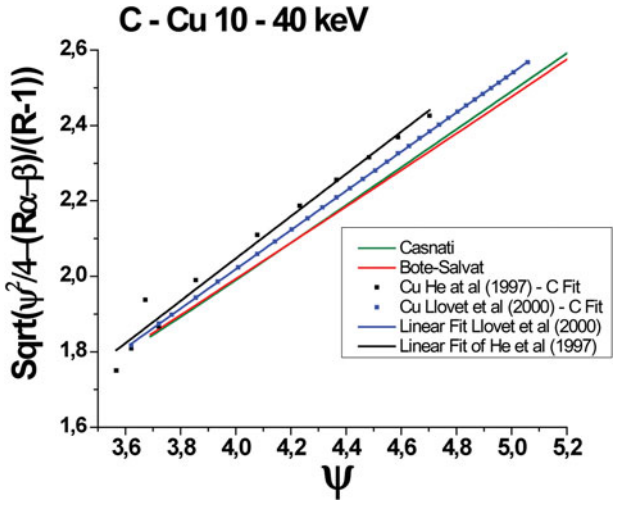

Figure 10. $\sqrt{\psi^2/4 - ((R_{A\text{-}B}^{E_2\text{-}E_1}\,\alpha - \beta)/(R_{A\text{-}B}^{E_2\text{-}E_1} - 1))}$ as a function of ψ, given by equations (31)–(34), with the $R_{\text{C-Cu}}^{E_0\text{-}E_1}$ values shown in Figure 8.

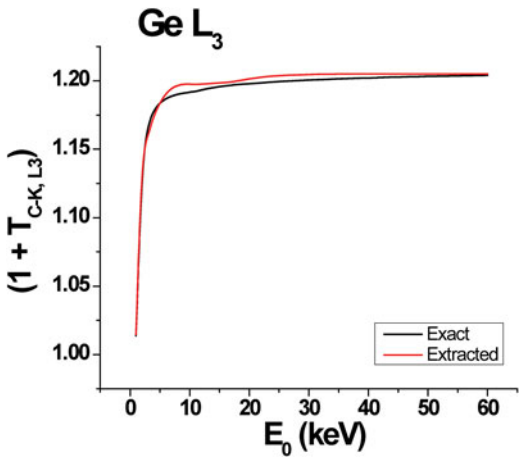

Figure 11. Coster-Kronig transition factors for the L_3 shell of Ge extracted from $R_{\text{C-Cu}}^{E_0\text{-}E_1}$ using equations (B.7)–(B.11) and compared with the exact values computed with equation (11).

Appendix B that its saturation at large overvoltage can be used to determine the Coster-Kronig Transition Factor $(1 + T_{CK,i})$. Figure 11 shows the Coster-Kronig transition factors for the L_3 shell of germanium computed with the method presented in Appendix B and the exact values computed with equation (11) (all the computational details are given in Appendix B). The agreement is excellent and shows the potential of using this method to determine Coster-Kronig transition factors for many elements, which will eventually lead to the development of accurate standardless quantitative methods, and also for the same elements in different compounds. This is because nonradiative transition depends on the band structure for low energy shells and if these variations are significant, this might invalidate the cancellation of this factor in classical ZAF analysis where the ratio of a given X-ray line is obtained from the specimen of unknown composition and the standard of known composition.

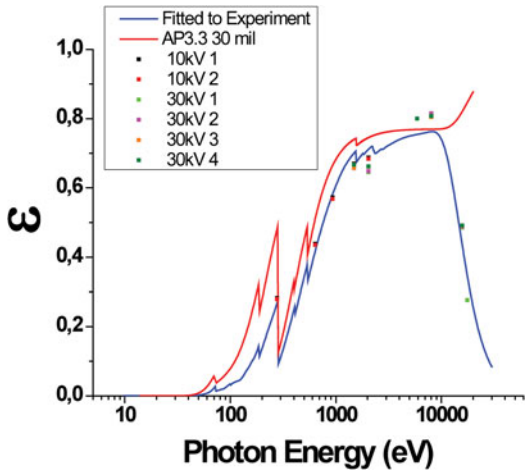

Figure 12. Detector efficiency of a SDD Oxford X-Max 80 mm^2 installed on a Hitachi SU-8000 cold-field FE-SEM measured with a specimen similar to that used by Alvisi et al. (2006) and calibrated with their EDS detector. Two spectra were acquired at 10 keV and four spectra were acquired at 30 keV, and the experimental detector efficiency, obtained with these spectra, is shown as single dots. Also shown is the nominal detector efficiency, labeled as AP3.3 and given by the manufacturer, and the fitted curve from the experimental data following the method described by Alvisi et al. (2006).

Measurement of the Detector Efficiency

Alvisi et al. (2006) have devised a method to measure experimentally the detector efficiency using an artificial mixture of carbon, aluminum, manganese, copper, and zirconium. The intensities of the characteristic lines of this material, I_i^0, were previously measured with an EDS detector of known detection efficiency, ε_i^0, calibrated in an X-ray synchrotron. When this material is inserted in another microscope that has a different EDS detector, the detector efficiency ε_i of element i can be computed as follows:

$$\varepsilon_i = \varepsilon_{\text{Mn}} \frac{I_i}{I_{\text{Mn}}} \left(\frac{\varepsilon_i^0 / \varepsilon_{\text{Mn}}^0}{I_i^0 / I_{\text{Mn}}^0} \right) \tag{38}$$

using the measured intensities, I_i, of the same material. It is interesting to note that the detector efficiency and the characteristic intensities are both normalized to the value of the K_α line of Mn. Because of the energy of this characteristic line, its transmission though the window of the detector and its absorption are very close to unity, and ε_{Mn} represents the transmission of the Si (or W) grid in front of a conventional polymeric window.

Figure 12 shows the detector efficiency of a silicon drift detector (SDD) Oxford X-Max 80 mm^2 (Oxford Instruments, Abingdon, Oxfordshire, UK) installed on a Hitachi SU-8000 cold-field FE-SEM (Hitachi, Ltd., Tokyo, Japan) measured with a specimen similar to that used by Alvisi et al. (2006) and calibrated with their EDS detector. Their experimental procedure was followed with two spectra acquired at 10 keV and four spectra acquired at 30 keV, and

the experimental values of detector efficiency, obtained with these spectra, are shown as single dots. Also shown is the nominal detector efficiency, labeled as AP3.3 and given by the manufacturer, and the fitted curve from the experimental data following the method described by Alvisi et al. (2006). In all of these curves, the nominal value of the transmission of X-rays through the grid (80%) was used for ε_{Mn}. Clearly, a strong difference between the experimental values and the nominal values of the detector efficiency is observed. This is due to the fact that the thicknesses of the various windows in front of the EDS detector are different from the nominal values, and this effect is clearly visible for photon energies below 2,000 eV. Above 10,000 eV, the strong disagreement between the nominal values and the measured ones is because the calculated values assumed an old Si(Li) detector with a Si crystal thickness of 3 mm where SDD detectors have much smaller thicknesses. Here, its determined value is 343 μm. It is obvious that accurate standardless X-ray microanalysis requires the measurement of the detector efficiency on every EDS detector with the method described by Alvisi et al. (2006). This should become a reality because in recent decades many countries have built state-of-the-art X-ray synchrotrons.

The Road toward Standardless X-Ray Microanalysis

What needs to be remembered is that standardless X-ray microanalysis, based on the ratio of characteristic lines of different elements taken from the same spectrum, always requires the computation of the Cliff and Lorimer $K_{A\text{-}B}$ factors and various corrections for the effect of absorption, fluorescence, and indirect X-ray generation by FSE and Auger electrons. Generally, the absorption correction is the most significant. The effects of FSE and Auger electrons on X-ray microanalysis are reviewed below.

To compute a Cliff and Lorimer $K_{A\text{-}B}$ factor, we need to compute ratios of the fundamental parameters, as seen in equation (13). With the measurement of various $R_{A\text{-}B}^{E_2\text{-}E_1}$ factors using equation (37), it will be possible to generate enough data to determine which models of ionization cross section are the best to compute the ratio and possibly to improve these models. Also, the measurement of $R_{A\text{-}B}^{E_2\text{-}E_1}$ factors with a K and L line will permit the determination of the Coster-Kronig transition factors of the corresponding L shell using the method presented in Appendix B. Using an M line instead of an L line will allow us to determine the Coster-Kronig transition factors of the corresponding M shell. Since this parameter is poorly known, this new method should be used extensively.

It is suggested that materials having elements that generate L and M lines should be ground to give particles with sizes below 50 nm, which should be deposited on a thin carbon film supported by a Be grid. The carbon film will give the desired K line but other elements with a K line could be present in the particles. A first X-ray spectrum should be obtained in a low magnification mode of imaging for a given beam energy E_1. The low magnification is expected to minimize effects of contamination and specimen drift. Then a second X-ray spectrum should be obtained at beam energy E_2 without moving the specimen and changing the magnification. Thus, $R_{A\text{-}B}^{E_2\text{-}E_1}$ can be computed using equation (37) because, by not moving the specimen, the composition of the particles will not have changed. The particles and the carbon film will need to be small enough to allow almost no beam spreading at these two beam energies and therefore the absorption correction will cancel out, as mentioned previously. Thus, by collecting spectra at different electron beam energies, many $R_{A\text{-}B}^{E_2\text{-}E_1}$ ratios will be measured without having to determine the specimen composition. The validation of the most accurate models to compute ionization cross section ratios and the determination of Coster-Kronig transition factors will then be possible.

The detector efficiency must be measured with a method similar to that of Alvisi et al. (2006). When the detector efficiency is measured for a given EDS detector, accurate experimental measurement of Cliff-Lorimer $K_{A\text{-}B}^{Exp}$ should be performed with a set of elements that span photons energies from 0.2 to 20 keV. Using the experimental values of the detector efficiencies obtained with a curve similar to that of Figure 12 for elements A and B, ε_A^{Exp} and ε_B^{Exp}, the calibration factor $\Lambda_{A\text{-}B}$ [defined in equation (26)] will be determined as follows:

$$\Lambda_{A\text{-}B} = K_{A\text{-}B}^{Exp} \frac{Q_A \omega_A \alpha_A A_B}{Q_B \omega_B \alpha_B A_A} \left[\frac{(1 + T_{CK,i})_A \varepsilon_A}{(1 + T_{CK,i})_B \varepsilon_B} \right]^{Exp} \tag{39}$$

with the experimental values of the Coster-Kronig transition factors determined using the new method presented in this article and the best choice of ionization cross sections deduced from $R_{A\text{-}B}^{E_2\text{-}E_1}$ ratio measurements. The main point here is that the measurement of the detector efficiency makes the calibration factor independent of the EDS detector used to measure it, allowing it to be used with any other EDS system for which the detector efficiency has been determined experimentally. Also, by choosing carefully the cross sections model and by measuring the Coster-Kronig transition factors, the calibration factors should reflect inconsistencies in the fluorescence yield and the weight of characteristic lines. This should significantly improve the accuracy of computed Cliff and Lorimer $K_{A\text{-}B}$ factors with the buildup of a database of $R_{A\text{-}B}^{E_2\text{-}E_1}$, $(1 + T_{CK,i})_i$ and $\Lambda_{A\text{-}B}$ for as many elements A and B as possible. With any EDS detector of known efficiency [determined with a method similar to that of Alvisi et al. (2006)], accurate Cliff and Lorimer $K_{A\text{-}B}$ factors will be computed as follows:

$$K_{A\text{-}B} = \Lambda_{A\text{-}B} \frac{Q_B \omega_B \alpha_B (1 + T_{CK,i})_B \varepsilon_B A_A}{Q_A \omega_A \alpha_A (1 + T_{CK,i})_A \varepsilon_A A_B}. \tag{40}$$

All the parameters in equation (40) will come from the database except the detector efficiency that will have to be determined experimentally, as stated previously. Note that with an accurate database of fundamental parameters and with good experimental $K_{A\text{-}B}$ factors, equation (40) could be

used to determine the detector efficiency and then compute accurate theoretical $K_{A\text{-}B}$ factors for a given EDS detector. Of course, only when the methods presented in this article have been used extensively to generate a huge database of fundamental parameters will true standardless quantitative X-ray analysis become possible.

Absorption Correction and Measurement of Specimen Thickness

When quantitative X-ray microanalysis is performed on an electron-transparent specimen, the specimen thickness must be known to compute the absorption correction, as shown in equation (16). In EELS, the specimen thickness is related to the ratio of the number of electrons that suffered inelastic collisions to the number of electrons that lost no energy and also to the inelastic mean free path, as demonstrated by Malis et al. (1988). The accuracy of this method is about 10–20% because of the uncertainties in the inelastic mean free path. The main problem of this method is that not all TEMs have an EELS and no SEM has one. The specimen thickness can also be determined using convergent beam techniques, but its applicability is limited to crystalline specimens. Also, not all TEMs can perform convergent beam analysis and it is not possible, yet, to use this technique in the SEM. This was the motivation of Watanabe and Williams (2006) to develop the ζ factor method to determine the specimen thickness with absolute X-ray measurement because most TEMs and SEMs have an EDS detector. However, the ζ factor method relies on the measurement of the probe current with a Faraday cup, and most TEMs and many SEMs do not have an integrated Faraday cup to allow such a measurement. Also, in cold-field electron microscopes, the probe current is drifting and such variations will introduce errors in using this method. Since there are more than 7,000 cold-field electron microscopes in the world (mostly SEMs), it is important to use a method that is not current-dependent because X-ray microanalysis in the STEM mode at 30 keV (and less for very thin objects) will become of paramount importance, as shown below in this article.

Since the STEM mode permits bright-field (BF) and dark-field (DF) imaging in the TEM and in the SEM, the ratio of the total intensity of both images will be independent of the probe current and will depend on the specimen thickness for a given composition. Figure 13 shows the ratio of the number of transmitted electrons that have an exit angle (relative to the incident beam direction) greater than 60 mRad $[N(\theta \geq 60 \text{ mRad})]$ to the number having an exit angle smaller than 20 mRad $[N(\theta \leq 20 \text{ mRad})]$, as a function of specimen thickness for carbon, aluminum, iron, silver, and gold at 100 keV. These curves were obtained using Monte Carlo simulations with the MC X-Ray program developed by Michaud and Gauvin (2009) with 1,000,000 simulated electron trajectories (with the exception of carbon where 10,000,000 trajectories were used). For all these elements, the ratio of this intensity increases with the specimen thickness, and the small fluctuations in the curves are statistical fluctuations coming from the Monte Carlo simulations. Also, there is a strong atomic number contrast using this ratio—two orders of magnitude of difference between C and Au. To use this method, calibration curves as a function of composition and specimen thickness will have to be computed, with Monte Carlo simulations, and the relation between the computed ratio of scattering angles to the ratio of intensities of DF to BF images (or high-angle annular dark field to bright field) will have to be calibrated with specimens of known composition and thickness. Of course, such calibration will not be necessary if the currents can be read directly from the BF and DF detectors. Then, an iterative method, similar to that of Watanabe and Williams (2006), will have to be developed to perform quantitative X-ray microanalysis with absorption correction for transparent specimens. Of course, for specimens that are transparent but where the conditions of validity of equation (16) do not hold, a quantitative X-ray method using the *f*-ratio technique with equations (26)–(27) will have to be developed with γ_i, given by equation (3) integrated from 0 to the specimen thickness. This is the case of transparent thick specimens and/or low incident electron energy, such as scanning TEM in the SEM at 30 keV and below. Models will have to be developed to compute the $\varphi(\rho z)$ curves where there is beam spreading in thin foils and energy loss.

Spatial Resolution for X-Ray Microanalysis

In this section, the spatial resolution for X-ray microanalysis will be reviewed because it is of crucial importance for the analyst to know the volume of the analyzed material for each spectrum produced. This is especially important for the acquisition of X-ray maps to avoid oversampling issues and also to interpret the data correctly. Bulk materials and thin film are considered here.

Spatial Resolution for Bulk Materials

Generally, the depth in a given bulk material where a characteristic X-ray is generated, X_G, is computed with the following equation:

$$X_G = \frac{k}{\rho}\,(E_0^n - E_c^n), \tag{41}$$

where ρ (the material density) and k are constants that depend on the atomic number of the irradiated material, E_0 is the incident electron energy, and E_c is the ionization energy of the electronic subshell of the characteristic line. The problem with this equation is that X-ray absorption is not taken into account, and the range of emitted X-rays, X_E, is smaller than X_G when X-ray absorption becomes significant. Gauvin (2007*a*) derived a universal equation to compute X_E by taking into account X-ray absorption:

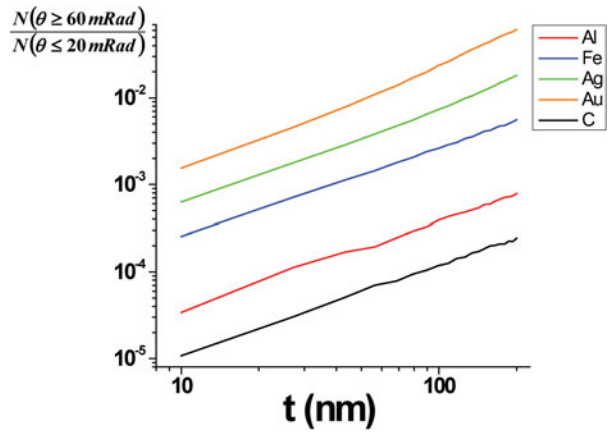

Figure 13. Ratio of the number of transmitted electrons having an exit angle (relative to the incident beam direction) greater than 60 mRad [$N(\theta \geq 60$ mRad)] to that having an exit angle smaller than 20 mRad [$N(\theta \leq 20$ mRad)] as a function of specimen thickness for carbon, aluminum, iron, silver, and gold at 100 keV. These curves were obtained using the Monte Carlo simulations with the MC X-Ray program developed by Michaud and Gauvin (2009) with 1,000,000 simulated electron trajectories (for each data point) except for carbon where 10,000,000 trajectories were used.

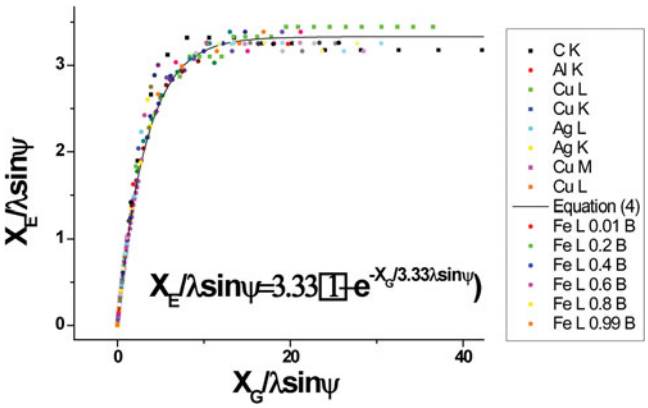

Figure 14. $X_E/\lambda \sin\psi$ as a function of $X_G/\lambda \sin\psi$ computed using equation (42) [mentioned as equation (4) in the legend of this graph] and also from Monte Carlo simulations of 200,000 electron trajectories (for each data point) in carbon, aluminum, iron, silver, and gold and an Fe-B alloy. This figure is taken from Gauvin (2007*a*).

$$X_E = \ln\left(\frac{1}{1-\alpha}\right) \times \lambda_X \sin\psi \left\{1 - \exp\left(-X_G \Big/ \ln\left(\frac{1}{1-\alpha}\right)\lambda_X \sin\psi\right)\right\}, \tag{42}$$

where λ_X is the mean free path for X-ray absorption of the characteristic line, ψ is the take-off angle of the X-ray detector and α is the fraction of X-rays that escape the specimen. For 95% of the X-rays that escape the specimen, $\ln(1/(1-\alpha))$ equals 3. Figure 14 shows $X_E/\lambda \sin\psi$ as a function of $X_G/\lambda \sin\psi$ computed with equation (42) for $\alpha = 0.964$ (96.4% of the X-rays escaping the specimen) and also from Monte Carlo simulations of 200,000 electron trajectories (for each data point) in carbon, aluminum, iron, silver, gold, and an Fe-B alloy, where 95% of the emitted X-ray were summed to compute X_E from the Monte Carlo simulations. These results show that equation (42) can be used to compute X_E and the interested reader is referred to the article of Gauvin (2007*a*) for the details of the derivation of this equation and also to find the equations needed to compute X_G and λ_X.

Spatial Resolution for Thin Foils

With the advent of field emission TEMs (FE-TEMs) with aberration correctors, a probe diameter of about 0.1 nm can be obtained routinely. The spatial resolution of EDS X-ray microanalysis therefore becomes limited by the beam broadening in the specimen and that is commonly evaluated with the single scattering equation derived by Goldstein et al. (1977). The beam broadening b, at the bottom of a thin foil, is the diameter that includes 90% of the scattered electrons and is given by

$$b = 6.25 \times 10^5 \frac{Z}{E_0}\sqrt{\frac{\rho}{A}}\, t^{3/2}\ (\text{cm}), \tag{43}$$

where Z is the atomic number of the thin film of thickness t (cm), ρ is the mass density (g/cm^3), A is the atomic weight (g/mole) of the thin film, and E_0 is the energy of the incident electrons (keV). The Goldstein equation assumes that a single elastic collision always occurs at the middle of the specimen, which overestimates the beam broadening for very thin specimens where most of the electrons will not scatter at all. Gauvin (2008) derived a single scattering equation that takes into account the probability of scattering for small thicknesses and also added a power law term to take into account plural scattering. Improved Monte Carlo simulations were performed since the publication of this article and better coefficients of the power law were obtained. The resulting beam broadening equation that includes 90% of the scattered electrons is (Gauvin, to be submitted for publication[b])

$$\frac{b}{2\lambda\theta^*} = \frac{\xi}{2} + [e^{-\xi} - 1] + \frac{1}{\xi}[1 - e^{-\xi}(1+\xi)] + 1.61 \times 10^{-3}\xi^{3.04}, \tag{44}$$

where $\xi = t/\lambda$, t being the specimen thickness, λ the elastic mean free path, and θ^* a characteristic scattering angle that is proportional to the screening parameter θ_0 and is given by the equation:

[b] Gauvin, R. A universal equation for computing the beam broadening of incident electrons in the electron microscope in a thin foil in the single scattering regime. To be submitted for publication to *Microscopy & Microanalysis*.

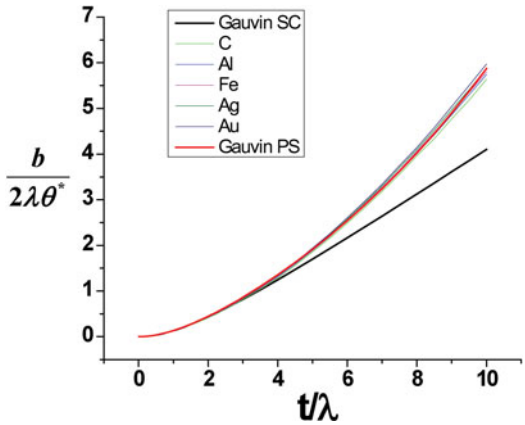

Figure 15. $b/2\lambda\theta^*$ versus t/λ for C, Al, Fe, Cu, and Au computed by Monte Carlo simulations with 1,000,000 electron trajectories (for each data point) for $E_0 = 100$ keV. Gauvin PS refers to the modeling of plural scattering, i.e., the whole equation (44) while Gauvin SC refers to the modeling of single scattering, i.e., equation (44) minus its last term, the power law equation.

$$\theta^* = 1.363 \frac{Z^{0.333}}{\sqrt{E_0}}, \tag{45}$$

where Z is, as usual, the atomic number of the material and E_0 is in keV. The article of Gauvin et al. (2006) gives the expressions to compute the elastic mean free path λ. The interested reader is referred to Gauvin (to be submitted for publication, see footnote b) for the complete derivation of equations (44) and (45).

Equation (44) predicts a universal curve when $b/2\lambda\theta^*$ is plotted as a function of t/λ. Figure 15 shows $b/2\lambda\theta^*$ versus t/λ for carbon, aluminum, iron, silver, and gold computed by Monte Carlo simulations with 1,000,000 electron trajectories (for each data point) for $E_0 = 100$ keV. Also shown in this figure is equation (44), labeled as Gauvin PS while Gauvin SC refers to the modeling of single scattering only, i.e., equation (44) minus its last term that is the power law term. Clearly, the universal behavior of equation (44) is seen with the normalized values of $b/2\lambda\theta^*$ computed by Monte Carlo simulations, the strongest differences being seen at $t/\lambda = 10$ and these are of $+2\%$ for gold and -4% for carbon. The universal behavior of equation (44) means that this equation is not dependent on a scattering model because the simulated data was normalized by the values of λ and θ_0 used in the Monte Carlo simulations. Therefore, this scattering model is not dependent on the choice of a given scattering model while the Goldstein equation is. Improved scattering models for λ and θ_0 could be used in equations (44) and (45) to compute more accurate values of b. It is also very interesting to note that the single scattering model of Gauvin (2008) is valid up to $t/\lambda = 3$.

Figure 16 compares $b/2\lambda\theta^*$ as a function of t/λ for equation (44) and also for equation (43) for carbon and gold. Equation (43) was normalized with the values of λ given by Gauvin et al. (2006) and with θ^* given by equation (45). For $t/\lambda < 1$, the Goldstein model overestimates the beam broadening because it assumes that there is always an elastic collision at the middle of the specimen, where in reality there is a probability of having an elastic collision that becomes smaller as t/λ decreases. For carbon, at $t/\lambda = 0.1$, the Goldstein model overestimates the beam broadening by 420% and by 807% for $t/\lambda = 0.01$. Equation (43) is often used to estimate the spatial resolution of X-ray microanalysis in variable pressure scanning electron microscopy (VP-SEM) where often $t/\lambda < 1$. As a result, the size of the skirt (the incident electrons scattered in the gas before hitting the specimen) is wrongly overestimated, giving a more pessimistic view of the capabilities of X-ray microanalysis in the VP-SEM. The Gauvin and Goldstein models are consistent around $t/\lambda = 1$, where one collision occurs but the Goldstein model underestimates the scattering above $t/\lambda > 1$, despite a slope that seems correct, because it assumes a single collision where there is more than one. The difference between $b/2\lambda\theta^*$ for C and Au computed with the Goldstein model is about 22.5%. The universal behavior already observed with the Monte Carlo simulations, as shown in Figure 15, is not observed with the Goldstein model. The paper of Gauvin (to be submitted for publication, see footnote b) gives more details about the derivation of equation (44) and its use, with many more results on this subject.

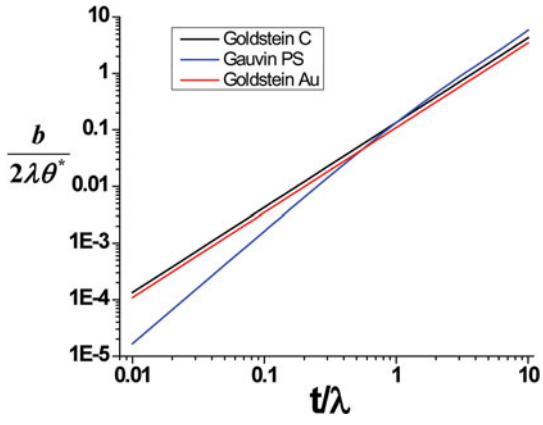

Figure 16. $b/2\lambda\theta^*$ as a function of t/λ for equation (44) (corresponding to Gauvin PS) and also for equation (43) for carbon and gold (corresponding to Goldstein). Equation (43) was normalized with the values of λ given by Gauvin et al. (2006) and with θ^* given by equation (45).

Effect of Fast Secondary Electrons and Auger Electrons on X-Ray Generation and Spatial Resolution

Fast secondary electrons (FSEs) are secondary electrons having an initial energy greater than 50 eV. Since their mean energy is about 2% of the energy of the incident electron (the electron that ionizes the atom leading to FSE generation), a 100 keV beam incident on a thin specimen in the TEM will generate FSEs, generally perpendicular to the beam with a mean energy of 2 keV. Figure 17 shows trajectories of FSEs, along with those of the primary beam, for graphite at 100 keV for a 30 nm thin foil. These were

Figure 17. Primary and FSE trajectories simulated by Gauvin (1990) in graphite at 100 keV for a thin foil of 30 nm.

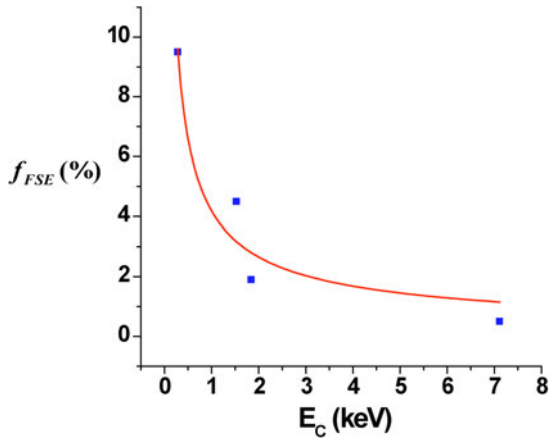

Figure 18. Percentage of X-rays generated by FSEs as a function of the ionization energy for the K shells of pure thin foils of C, Al, Si, and Fe at 100 keV. There results were obtained from Monte Carlo simulations by Joy et al. (1982).

simulated by Gauvin (1990). The FSEs travel much further in the thin film than do the primary electrons, and since they have much lower energy, they are more efficient in generating X-rays for light elements because of the increase in the ionization cross section. Also, they have enough energy to ionize the light elements in the major part of their path in the thin film. This effect was first pointed out by Joy et al. (1982) who performed Monte Carlo simulations to compute the percentage of X-rays generated by FSEs. Figure 18 shows the percentage of X-rays generated by FSEs as a function of the ionization energy for the K-shells of pure thin foils of C, Al, Si, and Fe at 100 keV. The percentage of X-rays generated by FSEs increases as the ionization energy of the ionized shell decreases for the reasons mentioned above—the lower the ionization energy of an element, the longer the FSE can ionize it during its path in the thin foil. About 10% of the X-rays are generated by FSEs for pure C and about 0.5% for pure Fe, which shows that X-rays generated by FSEs are significant for light elements. Gauvin (1990) developed a Monte Carlo program, using the model of Joy et al. (1982), to simulate the effect of the FSEs on the

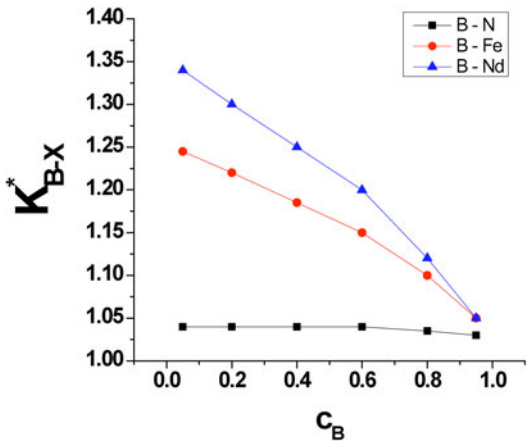

Figure 19. $K^*_{B\text{-}X}$ as a function of boron concentration, c_B, for B-N, B-Fe, and B-Nd systems for a primary beam of 100 keV and a 100 nm thick foil, computed by Gauvin and L'Espérance (1992) with primary electrons and FSE.

Cliff and Lorimer $K_{A\text{-}B}$ factor. In this regard, the normalized $K^*_{A\text{-}B}$ factor was defined as follows:

$$K^*_{A\text{-}B} = \frac{K_{A\text{-}B}(e_P + e_{FSE})}{K_{A\text{-}B}(e_P)}, \tag{46}$$

where $K_{A\text{-}B}(e_P + e_{FSE})$ is the Cliff and Lorimer $K_{A\text{-}B}$ factor computed with the X-rays generated by the primary electrons and by the FSEs and $K_{A\text{-}B}(e_P)$ is the Cliff and Lorimer $K_{A\text{-}B}$ factor computed with the X-rays generated by the primary electrons only. Any deviation of $K^*_{A\text{-}B}$ indicates that FSEs generate X-rays in the system A-B for given composition, specimen thickness, and beam energy. Also, it is easy to show that

$$K^*_{A\text{-}B} = \frac{1 - f_B}{1 - f_A}, \tag{47}$$

where f_i is the fraction of X-rays generated by FSEs for element i and it corresponds to f_{ind} in equation (2).

Figure 19 shows $K^*_{B\text{-}X}$ as a function of boron concentration, c_B, for B-N, B-Fe, and B-Nd systems with a primary beam of 100 keV and a 100 nm thick foil, as computed by Gauvin and L'Espérance (1992). For the B-N systems, the number of X-rays generated by FSEs is about the same and $K^*_{B\text{-}N}$ is close to 1 and not sensitive to c_B. However, for the B-Fe and B-Nd systems, the fraction of X-rays generated by Fe and Nd is negligible and $K^*_{B\text{-Fe}}$ and $K^*_{B\text{-Nd}}$ become sensitive to boron composition. Since FSEs lose energy when they travel and also because energy loss is a function of the specimen composition, the number of X-rays generated by FSEs becomes composition dependent for a system having a low energy line in addition to one of significantly higher energy. This means that in such cases equation (12) cannot be used to perform quantitative X-ray microanalysis because it assumes that $K_{A\text{-}B}$ is composition independent, which is true only if X-rays are generated by the primary electrons alone.

Figure 20 shows D_{90}, the diameter that includes 90% of the X-ray emission volume generated by the primary electrons and by the FSEs as a function of the accelerating

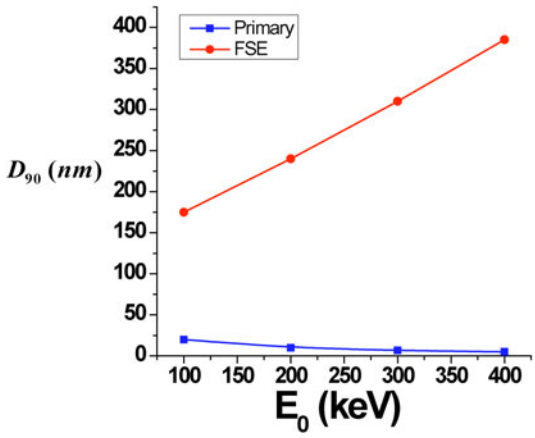

Figure 20. D_{90}, the diameter that includes 90% of the X-ray emission volume generated by the primary electrons and by the FSE, as a function of the accelerating voltage, E_0, for a 100 nm thick foil and a B-80 wt% Fe alloy, as calculated by Gauvin and L'Espérance (1992).

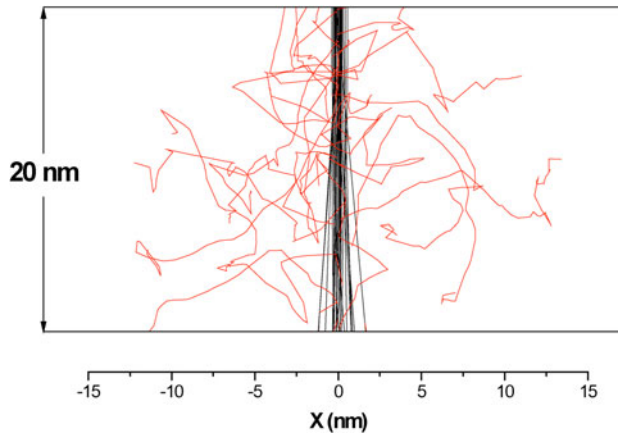

Figure 21. Trajectories of the primary and Auger Au $M_4N_{67}N_{67}$ electrons in a 20 nm thick foil of an Au–1% (at.) B alloy for E_0 = 100 keV. Taken from Gauvin (2007*b*).

voltage, E_0, for a 100 nm thick foil and a B–80 wt% Fe alloy, as calculated by Gauvin and L'Espérance (1992). As E_0 increases, the beam broadening of the primary electrons decreases, as expected, because the mean free path increases with E_0 and, specimen thickness being the same, t/λ becomes smaller and the beam broadening predicted by equation (44) becomes smaller. As E_0 increases, the FSEs have more initial energy and they can travel further in the specimen and D_{90} increases significantly. The degradation of spatial resolution of X-ray microanalysis using low energy lines in the TEM was also computed with Monte Carlo simulations by Romig et al. (1991). Therefore, the FSEs can significantly degrade the spatial resolution of X-ray microanalysis using low energy lines in the TEM. Gauvin et al. (1999) have shown that FSEs can also generate a significant number of X-rays for low energy lines in the SEM.

Gauvin (2007*b*) has studied the effect of Auger electrons on X-ray generation in thin foils of Au-B alloys. Figure 21 shows trajectories of the primary electrons and of Auger Au $M_4N_{67}N_{67}$ electrons in a 20 nm thick foil of an Au–1% (at.) B alloy for E_0 equal to 100 keV. Clearly, the trajectories of Auger electrons look similar to those of FSEs. However, the Auger Au $M_4N_{67}N_{67}$ electrons have incident energy of 2.1 keV, independent of the beam energy, while the FSEs have an initial energy distribution with a mean energy that increases with E_0. Therefore, different behavior in terms of X-ray generation and spatial resolution is to be expected. Figure 22 shows $K^*_{\text{B-Au}}$ as a function of the atomic fraction of boron, X_B, for an Au-B alloy in the form of foils of 10 and 100 nm with incident electron energy of 100 and 400 keV, including the effect of the Auger Au $M_4N_{67}N_{67}$ electrons on X-ray generation. $K^*_{\text{B-Au}}$ was computed using equation (47) with the fraction of B K_α X-rays generated by the Auger Au $M_4N_{67}N_{67}$ electrons simulated by Monte Carlo calculations. Clearly, $K^*_{\text{B-Au}}$ is a function of boron composition because the number of X-rays generated by the Auger electrons becomes more significant as the composition of boron decreases. As the boron concentration is reduced, more Auger Au $M_4N_{67}N_{67}$ electrons are produced, per boron atom, and the fraction of X-rays generated by these electrons increases for the K_α line of boron. Of course, the Auger Au $M_4N_{67}N_{67}$ electrons do not have enough energy to ionize the M-shell of Au, and they only affect the generation of the K_α line of boron, for this combination of elements. The variation of $K^*_{\text{B-Au}}$ with boron composition increases with specimen thickness and electron beam energy.

Figure 23 shows the radius of the volume of X-ray generation for the B K_α line generated by the primary electrons, the Auger Au $M_4N_{67}N_{67}$ electrons and both (labeled as Total) as a function of the beam energy, E_0, in an Au–1% (at.) B alloy for a specimen of thickness 10 nm and an incident probe diameter of 1 nm, computed by Gauvin (2007*b*) using Monte Carlo simulations. Above 100 keV, the Auger Au $M_4N_{67}N_{67}$ electrons significantly degrade the spatial resolution. The spatial resolution of the X-rays generated by the primary electrons equals only 1 nm. The spatial resolution equals 5 nm when the primary and Auger Au $M_4N_{67}N_{67}$ electrons are included, which corresponds to the effective resolution. Since the energy of Auger electrons does not change with E_0, the spatial resolution is constant above 100 keV. Below 50 keV, the spatial resolution is dominated by the scattering of the primary beam.

Since the effects of FSEs and Auger electrons presented here on the Cliff and Lorimer $K_{A\text{-}B}$ factor and on the spatial resolution of X-ray microanalysis were computed using Monte Carlo simulations, their experimental validation is urgently needed. $K^*_{A\text{-}B}$ can be measured experimentally with the measurement of $K_{A\text{-}B}(e_p)$ and $K_{A\text{-}B}(e_p + e_{FSE})$. $K_{A\text{-}B}(e_p)$ can be determined from a very small particulate of elements A and B where there will be no X-rays generated by FSEs and Auger electrons because they will escape the particulate. $K_{A\text{-}B}(e_p + e_{FSE})$ can be measured in a thin film of given thickness of the same system A-B, for various compositions. X-ray line scans will need to be measured across interfaces having light and heavy elements to validate the effect of FSEs and Auger electrons on spatial resolution. Comparison

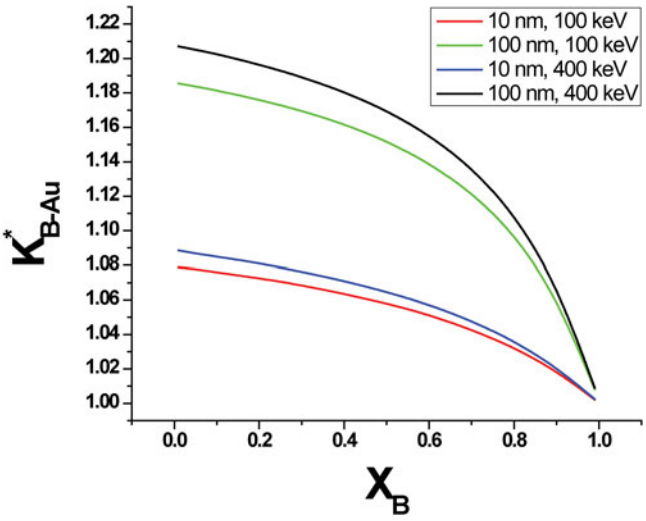

Figure 22. $K^*_{B\text{-}Au}$ as a function of the atomic fraction of boron, X_B, for a Au-B alloy using foils of 10 and 100 nm thicknesses with incident electron energy of 100 and 400 keV, including the effect of the Auger Au $M_4N_{67}N_{67}$ electrons on X-ray generation. Taken from Gauvin (2007*b*).

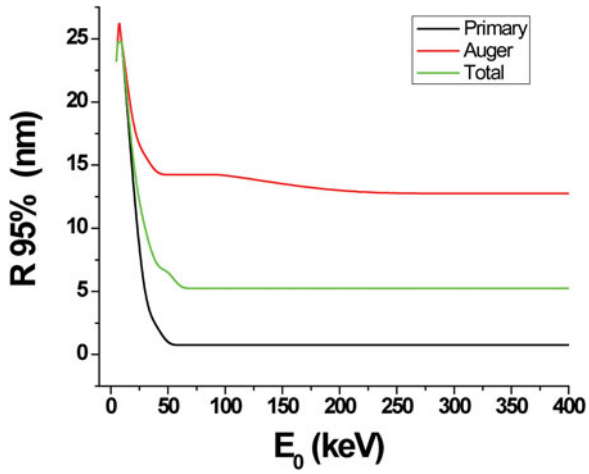

Figure 23. Radius of the volume of X-ray generation for the B K_α line generated by the primary electrons, the Auger Au $M_4N_{67}N_{67}$ electrons and both (labeled as Total) as a function of beam energy, E_0, in a Au–1% (at.) B alloy for a specimen of thickness 10 nm and an incident probe diameter of 1 nm. Taken from Gauvin (2007*b*).

with predictions based on Monte Carlo simulations will be necessary to determine if their effects are significant. This is very important, especially these days, with the new FE-TEMs equipped with aberration correctors. They are very expensive and their promise to give subnanometer spatial resolution for X-ray microanalysis is predicted on the basis of X-rays generated by primary electrons only. The predicted effect of FSEs and Auger electrons might limit the use of aberration-corrected microscopes to improve the spatial resolution in certain experimental situations, mostly for microanalysis involving low X-ray energy lines, and this needs to be clarified in the near future. Following this experimental validation, the quantitative models to perform

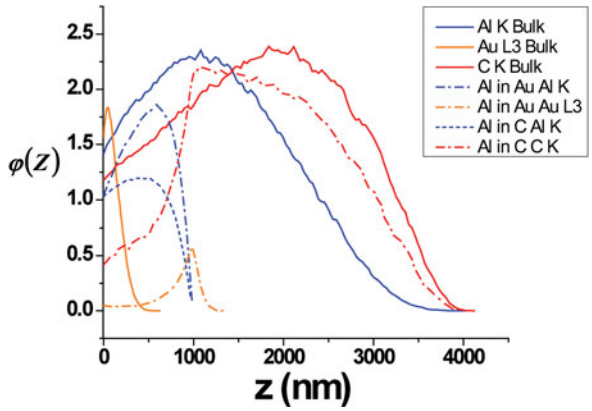

Figure 24. Curve of X-ray generation, $\varphi(z)$, as a function of the depth, z, for bulk Al, C, and Au and for an Al sphere of 1,000 nm diameter embedded in C and in Au. The center of the Al sphere is at a depth of 500 nm in both cases. These curves were simulated for incident electron energy of 20 keV with the Monte Carlo program MC X-Ray (Michaud & Gauvin, 2009). The $\varphi(z)$ curves for the K shells are shown for Al and C and for the L_3 shell for Au.

X-ray microanalysis will have to include their effect if they are found to be significant.

X-Ray Microanalysis of Heterogeneous Materials

The methods to convert X-ray intensities into concentrations, which were introduced above, are valid for specimens having homogeneous composition and flat surfaces. Following the pioneer work of Kyser and Murata (1974), quantitative schemes have been developed for the determination of the thickness and the composition of multilayered specimens by Pouchou (1993) and by Llovet and Merlet (2010). The work of Kyser and Murata (1974) inspired Gauvin (1990) (see also Gauvin et al., 1992) to develop a quantitative method for the microanalysis of spherical inclusions embedded in a matrix using Monte Carlo simulations. To perform quantitative X-ray microanalysis in these cases, the geometry of the material must be known in addition to the curve of X-ray generation as a function of depth, the $\varphi(\rho z)$ curve. For multilayered specimens, approximate analytical equations were developed. For more complicated geometries, only Monte Carlo simulations can give accurate $\varphi(\rho z)$ curves.

To demonstrate this point, Figure 24 shows curves of X-ray generation, $\varphi(z)$, as a function of the depth, z, for bulk Al, C, and Au and for an Al sphere of 1,000 nm diameter embedded in C and in Au. The center of the Al sphere is at a depth of 500 nm in both cases. These curves were simulated for incident electron energy of 20 keV using the Monte Carlo program MC X-Ray (Michaud & Gauvin, 2009). The $\varphi(z)$ curves for the K-shells are shown for Al and C and for the L3 shell for Au. $\varphi(z)$ curves are used here, instead of the $\varphi(\rho z)$ curves, because the material inside and outside the inclusion is different and does not have the same density, making discontinuities for ρz when an electron, or an X-ray, leaves the inclusion and enters the matrix. The concept of

$\varphi(\rho z)$ curves is therefore difficult to use for heterogeneous materials, and the $\varphi(z)$ curves should be used instead. Clearly, the $\varphi(z)$ curves of the embedded Al inclusion in C and in Au are very different from those of the bulk materials. It took almost 50 years for the scientific community to find a set of analytical equations to describe the $\varphi(\rho z)$ (or $\varphi(z)$) curves for bulk, homogeneous materials with an electron beam at normal incidence to a flat surface. It is therefore obvious that it would take much longer for the case of embedded spherical inclusions in a homogeneous matrix with a flat surface. The solution resides in using Monte Carlo simulations to simulate $\varphi(z)$ for X-rays generated from real materials. In fact, the Monte Carlo program MC X-Ray computes the $\varphi(x, y, z)$ curves with and without X-ray absorption directly in the simulation, permitting the computation of emitted X-ray intensities as a function of composition and geometrical parameters (like the diameter and the depth of an embedded inclusion in a matrix of a given composition). Also, more than one inclusion can be simulated with many different types of geometry (such as cubes and cylinders) and with different orientations.

It is often argued that Monte Carlo simulations are too slow and an unrealistically pessimistic view still exists with regard to this computational method. Computers are always becoming faster and, as an example, 70 electrons per second were simulated at 20 keV for the 1,000 nm Al inclusion in Au using MC X-Ray with a computer that has two Xeon® E5645 processors (Intel Corporation, Santa Clara, CA, USA) at 2.4 GHz. Perhaps these fast computers could be used to develop a database, from Monte Carlo simulations, of emitted X-rays for commonly used materials with a specific geometry, and subsequently an efficient and fast interpolation algorithm (between the already simulated X-ray intensities) could be used for live-time quantitative X-ray microanalysis. Therefore, the classical argument that Monte Carlo simulations are too slow no longer holds true, and significant progress to perform quantitative X-ray microanalysis will occur when this is recognized in the microanalysis community.

Conclusions

What remains to be done to allow quantitative X-ray microanalysis performed with EDS to become a true characterization technique? This article reviewed some of the most important tasks, in the opinion of its author. There is a strong need to measure the fundamental parameters for X-ray generation to develop accurate standardless quantitative methods. Using the ratio of characteristic lines acquired on the same X-ray spectrum, it was shown that the Cliff and Lorimer $K_{A\text{-}B}$ factor can be used in a general correction method that is appropriate for all types of specimens, as long as appropriate corrections for X-ray absorption, fluorescence, and indirect generation are included. Since the fundamental parameters appear in the $K_{A\text{-}B}$ factor, only the ratio of the ionization cross sections needs to be known, not their absolute values. In this regard, the measurement of ratios of $K_{A\text{-}B}$ factor (or intensities at different beam energies of the same material with almost no beam spreading in the material) will permit the validation of the best models to compute the ratio of ionization cross sections because this ratio gives the ratio of cross sections of two elements at two different energies. It was also shown, using this method, that the nonrelativistic Bethe equation to compute ratio of ionization cross section is very close to that computed with the equation of Casnati et al. (1982) and also to the ratio of cross sections computed with the equations proposed by Bote and Salvat (2008). That method was extended to show that it could be used to determine the value of the Coster-Kronig transitions factors, an important fundamental parameter for the generation of L and M lines, which are known with poor accuracy. The detector efficiency can be measured with specimens where the intensities had already been measured with an EDS detector, the efficiency of which was previously measured in an X-ray synchrotron (Alvisi et al., 2006). It is obvious that such specimens will become available and a world "round robin" should be initiated to generate a database of the fundamental parameters of X-ray generation with improved accuracy, leading to true standardless quantitative X-ray microanalysis.

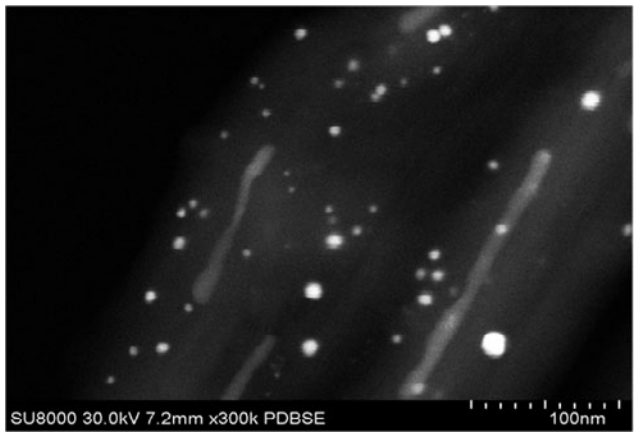

Figure 25. Backscattered electron image of multiwall carbon nanotubes covered with Pt particulates and with Fe rods inside the nanotubes. This picture was taken with a Hitachi SU-8000 FE-SEM. (Magnification 300,000×.)

The spatial resolution should always be computed when performing quantitative X-ray microanalysis and the equations for thin and bulk materials were presented. The effect of X-rays generated by FSEs and by Auger electrons will have to be measured experimentally because the Monte Carlo simulation results presented in this article show that their effect can be detrimental for the spatial resolution of materials involving low energy X-ray lines and also that the Cliff and Lorimer $K_{A\text{-}B}$ factor becomes composition dependent. Also, schemes to perform quantitative X-ray microanalysis of heterogeneous materials will need to use Monte Carlo simulations to develop the correction models. Finally, we should keep in mind that an EDS detector can be installed on any electron microscope, and we must develop quantitative methods in that respect. Figure 25 shows a

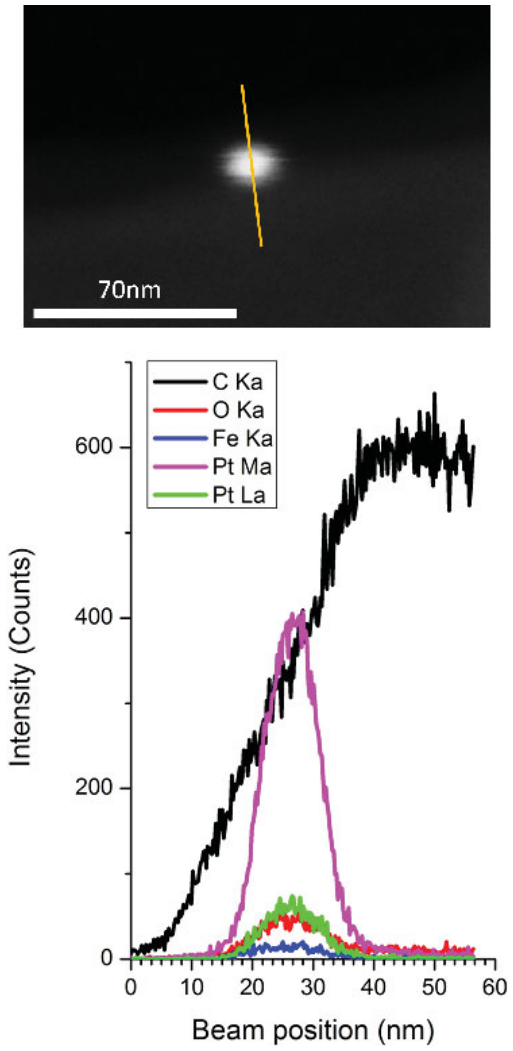

Figure 26. EDS line scan performed at 30 keV on a 20 nm Pt particulate obtained with an SDD EDS X-Max detector from Oxford installed on a Hitachi SU-8000 FE-SEM. The Pt M_α intensity (purple) clearly increases where the particulate is located. Also, an increase in Fe K_α (indigo) and O K_α (green) is observed at the particulate location. The C K_α intensity is in red.

backscattered electron image of multiwall carbon nanotubes covered with Pt particulates and with Fe rods inside the nanotubes. This was taken with a Hitachi SU-8000 field emission SEM. Pt particles as small as 1 nm are visible. Figure 26 shows an EDS line scan performed at 30 keV on a 20 nm Pt particulate obtained with an SDD EDS X-Max detector from Oxford installed on the same microscope. The Pt M_α intensity clearly increases where the particulate is located. Also, an increase in Fe K_α and O K_α is observed at the particulate location. The combination of an SDD detector and a high brightness gun gives a large number of generated and detected X-ray counts. The analytical capabilities of the new generation of FE-SEM are truly impressive, and the microanalytical community must work to develop a quantitative X-ray microanalysis method that works with all electron microscopes, especially the high-resolution ones, instead of saying "If you want to do quantitative X-ray microanalysis, buy the appropriate microscope," which might not always have the highest spatial resolution.

Acknowledgments

Nicolas Brodusch, from McGill University, Montréal, Canada is acknowledged for having determined the SDD EDS detector efficiency and for having taking the picture of Figure 25 and the X-ray data of Figure 26. Dr. Ysmael Verde, Instituto technologia de Cancun, Mexico, is acknowledged for providing us with the carbon nanotubes coated with the Pt particulates. Dr. Mathias Procop, IfG-Instite for Scientific Instruments (Berlin, Germany), is acknowledged for providing us with the calibrated specimen for the determination of the detector efficiency. Dr. Eric Lifshin, State University of New York at Albany (United States), is acknowledged for many useful comments concerning this work. Helen Campbell, from McGill University, is acknowledged for significant advice concerning this manuscript. Finally, the Canadian Foundation of Innovation, the National Science Engineering Research Council of Canada, and Le Fonds Québécois de Recherche en Sciences Naturelles et en Génie are acknowledged for financial support for this work.

References

Alvisi, M., Blome, M., Griepentrog, M., Hodoroaba, V.-D., Karduck, P., Mostert, M., Nacucchi, M., Procop, M., Rohde, M., Scholze, F., Statham, P., Terborg, R. & Thiot, J.-F. (2006). The determination of the efficiency of energy dispersive X-ray spectrometers by a new reference material. *Microsc Microanal* **12**, 406–415.

An, Z., Li, T.H., Wang, L.M., Xia, X.Y. & Luo, Z.M. (1996). Correction of substrate effect in the measurement of 8–25-keV electron-impact *K*-shell ionization cross sections of Cu and Co elements. *Phys Rev A* **54**(4), 3067–3069.

Anderson, I.A., Bentley, J. & Carter, C.B. (1995). The secondary fluorescence correction for X-ray microanalysis in the analytical electron microscope. *J Microsc* **178**(3), 226–239.

Bastin, G.F., Dijkstra, J.M. & Heijligers, H.J.M. (1998). PROZA96: An improved matrix correction program for electron probe microanalysis, based on a double gaussian $\varphi(\rho z)$ approach. *X-Ray Spectrom* **27**(1), 3–10.

Bote, D. & Salvat, F. (2008). Calculations of inner-shell ionization by electron impact with the distorted-wave and plane-wave Born approximations. *Phys Rev A* **77**, 042701.

Bote, D., Salvat, F., Jablonski, F. & Powell, C.J. (2009). Cross sections for ionization of K, L and M shells of atoms by impact of electrons and positrons with energies up to 1 GeV: Analytical formulas. *At Data Nucl Data Tables* **95**, 871–909.

Campbell, J.L. (2003). Fluorescence yields and Coster-Kronig probabilities for the atomic L subshells. *At Data Nucl Data Tables* **85**, 291–315.

Casnati, E., Tartari, A. & Baraldi, C. (1982). An empirical approach to K-shell ionization cross section by electron. *J Phys B* **15**, 155–167.

Castaing, R. (1951). Application of electron probes to local chemical and crystallographic analysis. PhD Thesis. Université de Paris.

Cliff, G. & Lorimer, G.W. (1975). The quantitative analysis of thin specimen. *J Microsc-Oxford* **103**, 203–207.

Colliex, C. & Jouffrey, B. (1972). Inelastic-scattering of electrons in a solid by excitation of deep atomic levels, Part 1, Energy-loss spectra. *Philos Mag* **25**(2), 491–498.

Davis, D.V., Mistry, V.D. & Quarles, C.A. (1972). Inner shell ionization of copper, silver and gold by electron bombardment. *Phys Lett A* **38**(3), 169–170.

Duncumb, P. (1957). Microanalysis with a scanning X-ray microscope. In *X-ray Microscopy and Microradiography*, Cosslet, V.E., Engstrom, A. & Pattee, H.H. (Eds.), p. 617. New York: Academic Press.

Egerton, R.F. (1975). Inelastic-scattering of 80 keV electrons in amorphous carbon. *Philos Mag* **31**(1), 199–215.

Egerton, R.F. (2011). *Electron Energy-Loss Spectroscopy in the Electron Microscope*, 3rd ed. New York: Springer.

Fischer, B. & Hoffmann, K.-W. (1967). Die Intensität der Bremsstrahlung und der charakteristischen*K*-Röntgenstrahlung dünner Anoden. *Z Physik* **204**(2), 122–128.

Fitzgerald, R., Kiel, K. & Heinrich, K. (1968). Solid-state energy-dispersion spectrometer for electron-microprobe X-ray analysis. *Science* **159**, 528.

Gauvin, R. (1990). Analyse chimique quantitative en microscopie électronique. PhD Thesis. Montréal, Canada: École Polytechnique de Montréal.

Gauvin, R. (1993). A parameterization of K-shell ionization cross section by electrons with an empirical modified Bethe's formula. *Microbeam Anal* **2**, 253–258.

Gauvin, R. (2007*a*). A universal equation for the emission range of X rays from bulk specimens. *Microsc Microanal* **13**(5), 354–357.

Gauvin, R. (2007*b*). The effect of auger electrons on X-ray microanalysis in the transmission electron microscope. *Microsc Microanal* **13**(S2), 1384–1385.

Gauvin, R. (2008). The spatial resolution of X-ray microanalysis with EDS in the transmission electron microscope. *Microsc Microanal* **14**(2), 1162–1163.

Gauvin, R., Drouin, D. & Hovington, P. (1999). The effect of FSE on X-ray microanalysis in the SEM. *Scanning* **21**, 238–245.

Gauvin, R. & L'Espérance, G. (1991). A new method for the determination of the C_{nl} parameter of the Bethe formula of ionization cross-sections based on the ratio of K factors obtained at different accelerating voltages. *J Microsc* **163**(3), 295–306.

Gauvin, R. & L'Espérance, G. (1992). A Monte Carlo code to simulate the effect of fast secondary electrons on K factors and spatial resolution in the TEM. *J Microsc* **168**(2), 153–167.

Gauvin, R., L'Espérance, G. & St-Laurent, S. (1992). Quantitative X-ray microanalysis of spherical inclusions embedded in a matrix using a SEM and Monte Carlo simulations. *Scanning* **14**, 37–48.

Gauvin, R., Lifshin, E., Demers, H., Horny, P. & Campbell, H. (2006). Win X-ray, a new Monte Carlo program that computes X-ray spectra obtained with a scanning electron microscope. *Microsc Microanal* **12**, 49–64.

Goldstein, J.I., Costley, J.L., Lorimer, G.W. & Reed, S.J.B. (1977). Quantitative X-ray analysis in the electron microscope. *Scan Electron Micros* **1**, 315–324.

Goldstein, J.I., Newbury, D.E., Joy, D.C., Lyman, C.E., Echlin, P., Lifshin, E., Sawyer, L.C. & Michael, J.R. (2003). *Scanning Electron Microscopy and X-Ray Microanalysis*. New York: Plenum Press.

He, F.Q., Peng, X.F., Long, X.G., Luo, Z.M. & An, Z. (1997). K-shell ionization cross sections by electron bombardment at low energies. *Nucl Instrum Methods B* **129**(4), 445–450.

Henoc, J. (1968). Quantitative electron probe microanalysis. NBS Special Publication 298. Washington, DC: National Bureau of Standards, U.S. Department of Commerce.

Hink, W. & Pashke, H. (1971*a*). *K*-shell-fluorescence yield for carbon and other light elements. *Phys Rev A* **4**, 507–511.

Hink, W. & Pashke, H. (1971*b*). Der Wirkungsquerschnitt für die Ionisierung der*K*-Schale von Kohlenstoff durch Elektronenstoß (2–30 keV). *Z Phys* **244**(2), 140–148.

Horny, P., Lifshin, E., Campbell, H. & Gauvin, R. (2010). Development of a new quantitative X-ray microanalysis method for electron microscopy. *Microsc Microanal* **16**(6), 821–830.

Hubbell, J.H. (1999). Compilation of photon cross-sections: Some historical remarks and current status. *X-ray Spectrom* **28**, 215–223.

Hubner, H., Ilgen, K. & Hoffman, K.-W. (1972). Messung des Wirkungsquerschnitts für Ionisierung in der*K*-Schale durch Elektronenstoß. *Z Phys* **255**(3), 269–280.

Isaacson, M. (1972). Interaction of 25 keV electrons with the nucleic acid bases, adenine, thymine, and uracil. II. Inner shell excitation and inelastic scattering cross sections. *J Chem Phys* **56**(5), 1813–1818.

Joy, D.C. (2001). Fundamental constants for quantitative X-ray microanalysis. *Microsc Microanal* **7**, 159–167.

Joy, D.C., Newbury, D.E. & Myklebust, R.L. (1982). The role of fast secondary electrons in degrading spatial resolution in the analytical electron microscope. *J Microsc-Oxford* **128**, RP1–RP2.

Kyser, D.F. & Murata, K. (1974). Qualitative electron microprobe analysis of thin films on substrate. *IBM J Res Develop* **18**, 352–363.

Llovet, X. & Merlet, C. (2010). Electron probe microanalysis of thin films and multilayers using the computer program XFILM. *Microsc Microanal* **16**(1), 21–32.

Llovet, X., Merlet, C. & Salvat, F. (2000). Measurements of K-shell ionization cross-sections of Cr, Ni and Cu by impact of 6.5–40 keV electrons. *J Phys B* **33**(8), 3761–3772.

Malis, T., Cheng, S.C. & Egerton, R.F. (1988). EELS log-ratio technique for specimen thickness measurement in the TEM. *J Electron Microsc Techniq* **8**, 193–200.

Merlet, C. (1994). An accurate computer correction program for quantitative electron probe microanalysis. *Mikrochim Acta* **114**, 363–376.

Merlet, C., Llovet, X. & Salvat, F. (2004). Measurements of absolute K-shell ionization cross sections and L-shell X-ray production cross sections of Ge by electron impact. *Phys Rev A* **69**(3), 032708.

Merlet, C., Llovet, X. & Salvat, F. (2008). Near-threshold absolute M-shell X-ray production cross sections of Au and Bi by electron impact. *Phys Rev A* **78**(2), 022704.

Michaud, P. & Gauvin, R. (2009). MC X-Ray, a new Monte Carlo program for quantitative X-ray microanalysis of real materials. *Microsc Microanal* **15**(S2), 488–489.

Newbury, D.E., Swyt, C.R. & Myklebust, R.L. (1995). Standardless quantitative electron probe microanalysis with energy dispersive X-ray spectrometry. Is it worth the risk? *Anal Chem* **67**(11), 1866–1871.

Nockolds, C., Cliff, G. & Lorimer, G.W. (1980). Characteristic X-ray fluorescence correction in thin film analysis. *Micron* **11**(3–4), 325–326.

Pia, M.G., Saracco, P. & Sudhakar, M. (2009). Validation of K and L shell radiative transition probability calculations. *IEEE Trans Nucl Sci* **56**(6), 3650–3661.

Pouchou, J.-L. (1993). X-ray microanalysis of stratified specimens. *Anal Chim Acta* **283**, 81–97.

Pouchou, J.-L. & Pichoir, F. (1984). A new model for quantitative X-ray microanalysis 1. Application to the analysis of homogeneous samples. *Recherche Aérospatiale* **3**, 167–192.

Powell, C.J. (1976). Cross sections for ionization of inner-shell electrons by electrons. *Rev Mod Phys* **48**, 33–47.

Reed, S.B.J. (1965). Characteristic fluorescence correction in electron-probe microanalysis, *Brit J Appl Phys* **16**, 913–926.

Romig, A.D., Michael, J.R. & Goldstein, J.I. (1991). X-ray spatial resolution at intermediate voltages: An assessment by massively parallel Monte Carlo electron trajectories simulations. In *Microbeam Analysis*, Howitt, D.G. (Ed.), pp. 119–126. San Francisco, CA: San Francisco Press.

Rossouw, C.J. & Whelan, M.J. (1979). The K-shell cross-section for 80 kV electrons in single-crystal graphite and AlN. *J Phys D* **12**, 797–807.

Schreiber, T.P. & Wims, A.M. (1981). A quantitative X-ray microanalysis method using K, L and M lines. *Ultramicroscopy* **6**, 323–334.

Shima, K. (1980). Mn and Cu K-shell ionization cross sections by slow electron impact. *Phys Lett A* **77**(4), 237–239.

Shima, K., Nakagawa, T., Umetani, K. & Fikumo, T. (1981). Threshold behavior of Cu-, Ge-, Ag-*K*-, and Au-L_3-shell ionization cross sections by electron impact. *Phys Rev A* **24**(1), 72–78.

Tawara, H., Harison, K.G. & De Heer, F.J. (1973). X-ray emission cross sections and fluorescence yields for light atoms and molecules by electron impact. *Physica* **63**(2), 351–367.

Watanabe, M. & Williams, D.B. (2006). The quantitative analysis of thin specimens: A review of progress from the Cliff-Lorimer to the new ζ-factor methods. *J Microsc* **221**(2), 89–109.

Westbrook, G.L. & Quarles, C.A. (1987). Total cross sections for ionization of the K-shell by electron bombardment. *Nucl Instrum Meth B* **24–25**(1), 196–198.

Wood, J.E., Williams, D.B. & Goldstein, J.I. (1984). Experimental and theoretical determination of $K_{A\text{-}Fe}$ factors for quantitative X-ray microanalysis in the analytical electron microscope. *J Microsc* **133**, 255–274.

Zaluzec, N.J. (1984). K and L shell cross sections for X-ray microanalysis in an AEM. In *Analytical Electron Microscopy*, Geiss, R.H. (Ed.), pp. 279–284. San Francisco, CA: San Francisco Press.

Appendix A: Computation of $R_{A\text{-}B}^{E_2\text{-}E_1}$ with Linear Curve Fitting Parameters

Assuming that $\sqrt{\psi^2/4 - ((R_{A\text{-}B}^{E_2\text{-}E_1}\alpha - \beta)/(R_{A\text{-}B}^{E_2\text{-}E_1} - 1))}$ as a function of ψ is linear, equation (31) has to be rewritten as

$$\sqrt{\frac{\psi^2}{4} - \frac{(R_{A\text{-}B}^{E_2\text{-}E_1}\alpha - \beta)}{R_{A\text{-}B}^{E_2\text{-}E_1} - 1}} = m\psi + \ln(c_{nl}) \tag{A.1}$$

and solving for $R_{A\text{-}B}^{E_2\text{-}E_1}$ gives

$$R_{A\text{-}B}^{E_2\text{-}E_1} = \frac{\psi^2(m^2 - \frac{1}{4}) + \beta + \ln^2(c_{nl}) + 2m\psi\ln(c_{nl})}{\psi^2(m^2 - \frac{1}{4}) + \alpha + \ln^2(c_{nl}) + 2m\psi\ln(c_{nl})}. \tag{A.2}$$

Therefore, with any values of m and c_{nl} obtained from linear regression analysis of the plot of $\sqrt{\psi^2/4 - ((R_{A\text{-}B}^{E_2\text{-}E_1}\alpha - \beta)/(R_{A\text{-}B}^{E_2\text{-}E_1} - 1))}$ as a function of ψ, values of $R_{A\text{-}B}^{E_2\text{-}E_1}$ can be computed accurately with equation (A.2) if a linear behavior is observed. Equation (A.2) can be used in equation (35) to compute the $K_{A\text{-}B}$ factor at electron beam energy E_2 from an experimental one measured at a beam energy E_1. Putting $m = 1/2$ in equation (A.2) yields

$$R_{A\text{-}B}^{E_2\text{-}E_1} = \frac{\beta + \ln^2(c_{nl}) + \psi\ln(c_{nl})}{\alpha + \ln^2(c_{nl}) + \psi\ln(c_{nl})}, \tag{A.3}$$

which becomes equivalent to equation (30) when equations (32)–(34) are inserted and the Bethe theory is recovered.

Appendix B: Determination of the Coster-Kronig Transition Factors

In the case where a K_α line is used for element A and an L_α line for element B, insertion of equation (13) into equation (28) gives

$$R_{A\text{-}B}^{E_2\text{-}E_1} = \frac{Q_B^{E_2} Q_A^{E_1} (1 + T_{CK,L_3})_B^{E_2}}{Q_B^{E_1} Q_A^{E_2} (1 + T_{CK,L_3})_B^{E_1}}. \tag{B.1}$$

The key point is that the ratio of the Coster-Kronig Transitions Factor is constant above 20 to 30 times the ionization energy of the L_3 shell, $E_c^{L_3}$. By defining Γ_{CK} as

$$\Gamma_{CK} = \frac{(1 + T_{CK,L_3})_B^{E_2}}{(1 + T_{CK,L_3})_B^{E_1}} \tag{B.2}$$

for $E_2 \geq 30E_c^{L_3}$, it can be determined with a measured $(R_{A\text{-}B}^{E_2\text{-}E_1})^{Mes}$ factor at high E_2 ($E_2 \geq 30E_c^{L_3}$) and a choice of a model to compute the ionization cross sections that is known to give accurate $R_{A\text{-}B}^{E_2\text{-}E_1}$ ratios. Insertion of equation (B.2) into equation (B.1) gives

$$\Gamma_{CK} = \frac{(R_{A\text{-}B}^{E_2\text{-}E_1})^{Mes}}{\dfrac{Q_B^{E_2} Q_A^{E_1}}{Q_B^{E_1} Q_A^{E_2}}}. \tag{B.3}$$

The next step is to use $(R_{A\text{-}B}^{E_2\text{-}E_1})^{Mes}$ and Γ_{CK} to calculate the values of the ratio of the cross sections for $E_2 \geq 30E_c^{L_3}$ by extrapolation. To do so, $(R_{A\text{-}B}^{E_2\text{-}E_1})^{Mes}$, measured for $E_2 \geq 30E_c^{L_3}$, must be fitted and equation (A.1) must be modified because there is some small deviation from linearity in the plots that are visible in Figures 9b and 9c. These small deviations in the interpolation range become more significant when extrapolation is performed, especially for extrapolated values near E_1. For that reason, equation (A.1) is generalized in this way:

$$\sqrt{\frac{\psi^2}{4} - \frac{((R_{A\text{-}B}^{E_2\text{-}E_1})^{Mes}\alpha - \beta)}{(R_{A\text{-}B}^{E_2\text{-}E_1})^{Mes} - 1}} = f(\psi), \tag{B.4}$$

where $f(\psi)$ is any suitable function that fits the data well. Solution of equation (B.4) gives the fitted $(R_{A\text{-}B}^{E_2\text{-}E_1})^{Fit}$ factor as

$$(R_{A\text{-}B}^{E_2\text{-}E_1})^{Fit} = \frac{[f(\psi)]^2 - \dfrac{\psi^2}{4} + \beta}{[f(\psi)]^2 - \dfrac{\psi^2}{4} + \alpha}. \tag{B.5}$$

The most natural choice to include the nonlinear effect is to use a second-order polynomial and $f(\psi)$ is given by this equation:

$$f(\psi) = \ln(c_{nl}) + m\psi + d\psi^2. \tag{B.6}$$

The next step is to use $(R_{A\text{-}B}^{E_2\text{-}E_1})^{Fit}$ at $E_2 \geq 30E_c^{L_3}$ to compute the extrapolated ratio of the ionization cross sections as follows:

$$\left(\frac{Q_B^{E_2} Q_A^{E_1}}{Q_B^{E_1} Q_A^{E_2}}\right)^{Extr} = \frac{1}{\Gamma_{CK}} \frac{[\,f(\psi)]^2 - \dfrac{\psi^2}{4} + \beta}{[\,f(\psi)]^2 - \dfrac{\psi^2}{4} + \alpha}, \tag{B.7}$$

where equation (B.5) was inserted in equation (B.3). Then, the ratio of the Coster-Kronig transition factors can be determined for $E_2 < 30E_c^{L_3}$ as follows:

$$\frac{(1 + T_{CK,L_3})_B^{E_2}}{(1 + T_{CK,L_3})_B^{E_1}} = \frac{(R_{A\text{-}B}^{E_2\text{-}E_1})^{Mes}}{\left(\dfrac{Q_B^{E_2} Q_A^{E_1}}{Q_B^{E_1} Q_A^{E_2}}\right)^{Extr}} \tag{B.8}$$

with $(R_{A\text{-}B}^{E_2\text{-}E_1})^{Mes}$ measured for $E_2 < 30E_c^{L_3}$. The slope, m, of the ratio of the Coster-Kronig factors above E_1 can be computed as follows:

$$m \cong \frac{(1 + T_{CK,L_3})_B^{E_1+\Delta E} - (1 + T_{CK,L_3})_B^{E_1}}{(1 + T_{CK,L_3})_B^{E_1} \Delta E} \tag{B.9}$$

and assuming that the slope from $E_c^{L_3}$ to E_1 is the same as that from E_1 to $E_1 + \Delta E$ and by taking the difference in the numerator of equation (B.9) from E_1 to $E_c^{L_3}$, we obtain

$$m \cong \frac{(1 + T_{CK,L_3})_B^{E_1} - (1 + T_{CK,L_3})_B^{E_c^{L_3}}}{(1 + T_{CK,L_3})_B^{E_1} \Delta E}. \tag{B.10}$$

Knowing that $(1 + T_{CK,L_3})_B^{E_c^{L_3}} = 1$, by definition, solution of equation (B.10) for $(1 + T_{CK,L_3})_B^{E_1}$ gives

$$(1 + T_{CK,L_3})_B^{E_1} = \frac{1}{1 - m(E_1 - E_c^{L_3})} \tag{B.11}$$

and the absolute values of the Coster-Kronig transition factors can be determined with the ratios computed with equation (B.8).

To test this new method, $R_{A\text{-}B}^{E_2\text{-}E_1}$ was computed for the K shell of carbon and the L_3 shell of germanium using equation (B.1) for electron energy E_2 between 1.3 and 60 keV and E_1 equal to 1.3 keV. The Bote et al. (2009) equations to compute the ionization cross sections were used in equation (B.1) and in equation (11) to compute the Coster-Kronig transition factors of the L_3 shell of germanium. Also, the same parameters used in Figure 4 were used to compute the $(1 + T_{CK,L_3})$ ratios with equation (11) and inserted in equation (B.1). These computed $R_{C\text{-}Ge}^{E_2\text{-}E_1}$ ratios were fitted with equations (B.4) and (B.6), with E_2 between 40 to 60 keV, as shown in Figure B.1. The values of the coefficients obtained are the following: $\ln(c_{nl}) = -0.00344$, $m = 0.49566$,

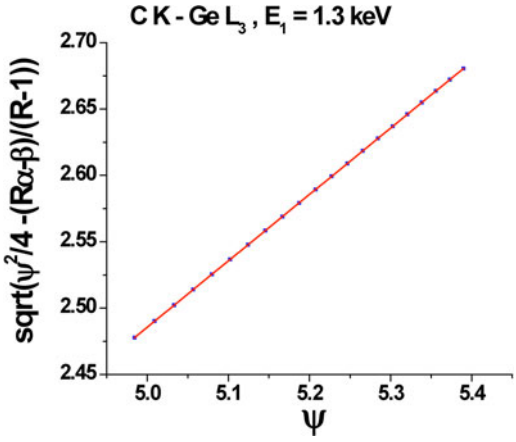

Figure B.1. $\sqrt{\psi^2/4 - ((R_{A\text{-}B}^{E_2\text{-}E_1}\alpha - \beta)/(R_{A\text{-}B}^{E_2\text{-}E_1} - 1))}$ as a function of ψ, given by equation (31)–(34), with the $R_{C\text{-}Ge}^{E_2\text{-}E_1}$ values computed with the Bote-Salvat ionization cross sections [equations (8)–(10)] where E_2 is between 40 and 60 keV and $E_1 = 1.3$ keV for the K shell of C and the L_3 shell of Ge. The full line was fitted with equations (B.4) and (B.6).

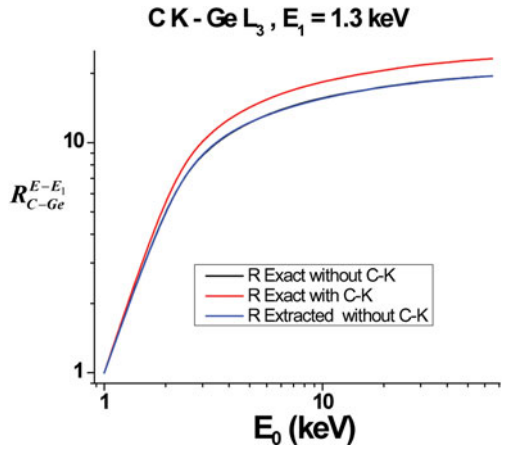

Figure B.2. $R_{C\text{-}Ge}^{E_2\text{-}E_1}$ computed exactly with and without the Coster-Kronig transition factors, equations (B.1) and (29), respectively, for the K shell of C and the L_3 shell of Ge. Also, the ratio of the ionization cross sections computed with equation (B.7) (corresponding to $R_{C\text{-}Ge}^{E_2\text{-}E_1}$ extracted without C-K) is shown.

and $d = 4.28461e - 4$ with $R^2 = 1$. It is clear that the deviation from linearity is not very significant in the interpolation region, but the second-order term is needed to use equation (B.5) at low values of E_2 to compute accurate ratios of ionization cross sections. This is shown in Figure B.2, which compares $R_{C\text{-}Ge}^{E_2\text{-}E_1}$ computed with [equation (B.7)] and without the Coster-Kronig transition factors [equation (B.5)]. Clearly, the method presented here to compute this ratio by extrapolation seems to works very well. Figure 11 shows the Coster-Kronig transition factors computed with equations (B.5) to (B.11) with the exact values computed with equation (11). The agreement is excellent. Also, the agreement can certainly be improved by finding the optimum condition of the fit [energy range E_1 and E_2, the number of points and the choice of $f(\psi)$ in equation (B.4)]. Work in this regard is currently being performed.